


RESEARCH

Open Access



Petrophysical characterization, BIB-SEM imaging, and permeability models of tight carbonates from the Upper Jurassic (Malm β), SE Germany

Simon Freitag^{1*} , Jop Klaver^{2,5}, Iulian S. Malai^{2,3}, Norbert Klitzsch⁴, Janos L. Urai^{2,6}, Harald Stollhofen¹, Wolfgang Bauer¹ and Joyce Schmatz^{2,5}

*Correspondence:
simon.s.freitag@fau.de

¹ GeoZentrum Nordbayern, Friedrich-Alexander-Universität (FAU) Erlangen-Nürnberg, Schlossgarten 5, 91054 Erlangen, Germany

² Structural Geology, Tectonics and Geomechanics, RWTH Aachen University, Lochnerstrasse 4-20, 52064 Aachen, Germany

³ Present Address: Shearwater GeoServices, 77 Mount Ephraim, Brockbourne House, Tunbridge Wells, Kent TN4 8BS, UK

⁴ Applied Geophysics and Geothermal Energy (E.ON Energy Research Center), RWTH Aachen University, Mathieustraße 10, 52074 Aachen, Germany

⁵ Present Address: MaP-Microstructure and Pores GmbH, Junkerstrasse 93, 52064 Aachen, Germany

⁶ GeoStructures Consultancy for Structural Geology and Geomechanics, Maastricht, The Netherlands

Abstract

Tight carbonate rocks are important hydrocarbon and potential geothermal reservoirs, for example, in CO₂-Enhanced Geothermal Systems. We report a study of outcrop samples of tectonically undeformed tight carbonates from the upper Jurassic “Malm β ” formation in Southern Germany near the town of Simmelsdorf (38 km NE of Nuremberg) to understand bulk petrophysical properties in relation to microstructure and to compare models for permeability prediction in these samples. We applied Archimedes isopropanol immersion, Helium pycnometry, mercury injection, gamma density core logging, and gas permeability measurements, combined with microstructural investigations and liquid metal injection (LMI-BIB-SEM). In addition, ultrasonic velocity was measured to allow geomechanical comparison of stratigraphically equivalent rocks in the South German Molasse Basin (SGMB). Results show only small variations, showing that the formation is rather homogeneous with bulk porosities below 5% and argon permeabilities around 1.4E–17 m². The presence of stylolites in some of the samples has neither a significant effect on porosity nor permeability. Pores are of submicron size with pore throats around 10 nm and connected as shown by Mercury injection and Liquid Metal injection. Samples have high dynamic Young’s Modulus of 73 ± 5 GPa as expected for lithified and diagenetically overmature limestones. Moreover, no trends in properties were observable toward the faults at meter scale, suggesting that faulting was post-diagenetic and that the matrix permeabilities were too low for intensive post-diagenetic fluid–rock interaction. Petrophysical properties are very close to those measured in the SGMB, illustrating the widespread homogeneity of these rocks and justifying the quarry as a reasonable reservoir analog. Permeability prediction models, such as the percolation theory-based Katz-Thompson Model, Poiseuille-based models, like the Winland, the Dastidar, the capillary tube, and the Kozeny-Carman Models, as well as several empirical models, namely, the Bohnsack, the Saki, and the GPPT Models, were applied. It is shown that the capillary tube Model and the Saki Model are best suited for permeability predictions from BIB-SEM and mercury injection capillary pressure results, respectively, providing a method to estimate permeability in the subsurface from drill

cuttings. Matrix permeability is primarily controlled by the pore (throat) diameters rather than by the effective porosity.

Keywords: Porosity, Limestone, Permeability, Permeability models, Malm, Geomechanics

Introduction

The energy transition requires exploration for unconventional renewable energy sources, such as Enhanced Geothermal Systems (EGS), where hydraulically active fracture corridors are created by hydraulic and chemical stimulation techniques (Stober and Bucher 2013). Here, tight but thermally highly conductive carbonate rocks bear the potential of playing a vital role in the energy transition (e.g., Gosnold et al. 2010; Hofmann et al. 2014). Such reservoirs are characterized by very low matrix permeabilities, typically in the range of 0.001–10 mD (Akanji et al. 2013), implying that fluid transport in low-permeable or tight carbonate rocks is focused to fractures and faults (Al-Obaid et al. 2005; Dimmen et al. 2017; Litsey et al. 1986; O'Neill 1988; Zeybeck and Kuchuk 2002) with only minor fluid flow through the rock matrix (Bohnsack et al. 2020, 2021). However, microporosity and structures may impact fracture pattern, fracture density, fracture propagation, well logging (e.g., PHI, acoustic log, neutron log), and fluid losses, and thus the effectivity of carbonate matrix stimulation treatments (Barri et al. 2021; Ziauddin and Bize 2007).

A major aquifer in southern Germany is the Upper Jurassic (Malm) limestone reservoir from which geothermal energy for electricity and/or heat supplies is currently (August 2022) produced by >22 geothermal power plants in the South German Molasse Basin (SGMB) (Moeck et al. 2019; Weber et al. 2019). As geophysical borehole measurements or cores from this low-permeable thermal aquifer are scarce, incomplete, or even non-existent (Bohnsack et al. 2020, 2021), petrophysical investigations of rock samples from stratigraphically equivalent reservoir analogs are common practice. The tight carbonates of the Upper Jurassic Malm β carbonates exposed in the Frankenalb of Northern Bavaria (Fig. 1) are part of the same stratigraphic unit as the producing geothermal aquifer in the SGMB. In terms of lithofacies, the Malm β carbonates in South Germany predominantly classify as mud- to wackestones (Koch et al. 2005). These units of which maximum burial depth of c. 1100 m has been recently determined represent an excellent opportunity to acquire and compare petrophysical macro- and microstructural parameters of reservoir analogs to geothermal target lithologies in the Munich area of the SGMB 100–200 km to the south, where a similar burial depth was reached (Freitag et al. 2022). From a number of available natural and artificial outcrops we chose a study area NE of Nuremberg (Fig. 1).

The primary goal of this study is to characterize the tight carbonate rocks in terms of their structural anisotropy, their petrophysical and microstructural properties, and the lateral and vertical variability of these parameters. Secondly, by understanding heterogeneities we aim to improve estimates of the contribution of fluid transport between matrix and fracture system at the scale of our field lab (c. 32 × 34 m) and for modeling purposes. As pore systems in tight carbonates are primarily controlled by lithofacies and later modified by diagenetic and tectonic processes (Haines et al. 2016), the petrophysical properties and pore characteristics of the matrix of faulted carbonate rocks are

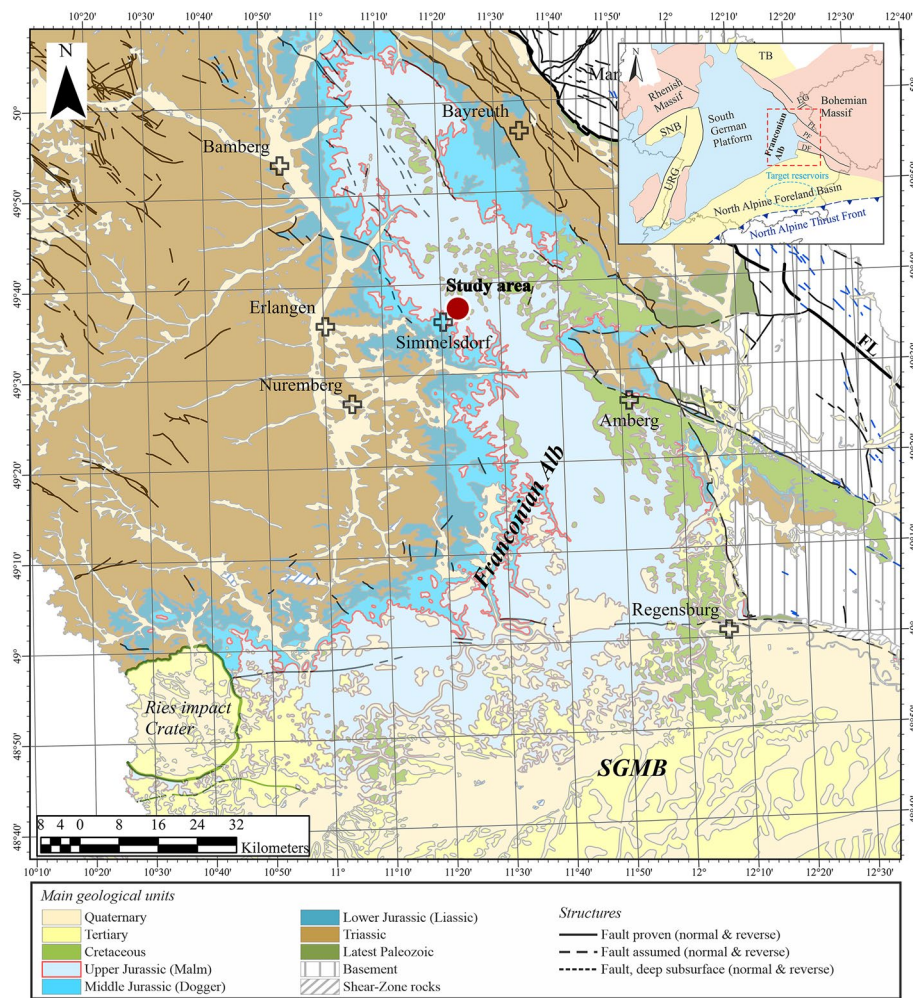


Fig. 1 Geological map of northern Bavaria, showing major stratigraphic units, structural features, and the test field location ~ 38 km NE of Nuremberg. Background data source: Bayerisches Landesamt für Umwelt, www.lfu.bayern.de. The city data (transparent crosses) were provided by <https://mapcruzin.com/> (downloaded: 19 July 2021 at 9:45). The administrative region data belong to © GeoBasis-DE/BKG (2021)

assessed. We also investigate the hydraulic influence of stylolites, which tend to form either barriers (Rashid et al. 2017) or conduits for fluid flow (Bruna et al. 2019). Consequently, stylolites are thought being responsible for most of the variability in petrophysical properties in these rock types (Bruna et al. 2019).

Previous studies focused on a lithofacies-dependent thermophysical and simple petrophysical characterization (porosity and permeability) of core and cutting samples of the Upper Jurassic reservoir (Malm β) in the SGMB and their outcrop analogs in the Northern and Southern Franconian Alb (Homuth et al. 2014, 2015). A similar study, though including geomechanical measurements as well as a petrographic study, was conducted by Mraz et al. (2018) on outcrop reservoir analog samples from the Southern Franconian Alb. Bohnsack et al. (2020, 2021) conducted extensive studies investigating potential lithofacies-dependent porosity–permeability relationships of Upper Jurassic limestones (i.e., Malm α and β) and their stress sensitivity (Malm ζ) within the SGMB. Potten et al. (2019) and Potten (2020), on the other hand, characterized Upper Jurassic

limestones derived from both the subsurface (243–5225 m TVD) of the SGMB and from outcrops ~40 km N of our test area in terms of their geomechanical properties. Taking this a step further our paper additionally evaluates the strength of Franconian Alb reservoir analog samples and we discuss to which degree their petrophysical properties are applicable to buried reservoir rocks of the same stratigraphic units in the SGMB. By applying a combination of state-of-the-art direct, indirect, and graphical methods, we try to achieve more comprehensive understanding of factors that are primarily controlling fluid flow within the rock matrix so that more reliable permeability predictions can be made.

A second aim is more technical. As for many geothermal reservoirs only a limited number of samples is available, petrophysical data of the target rock formation determined from cuttings are essential for subsequent reservoir quality evaluation and modeling. Plug ends, that result from preparing the plug cores in the quarry compared to cuttings in terms of their relatively small size, are investigated by combined mercury intrusion capillary pressure (MICP) measurements and broad ion beam scanning electron microscopy (BIB-SEM). Based on MICP measurements, bulk information on quantitative pore characteristics are obtained, including the pore throat size distribution, down to a pore throat size of only 3 nm (Clarkson et al. 2013; Giesche 2006; Okolo et al. 2015; Webb 2001; Xu et al. 2018a, b; Zhao et al. 2018). A variety of models enable permeability estimation based on MICP data. Therefore, this method is considered as a standard for the investigation of tight reservoir rocks (Gao et al. 2016; Okolo et al. 2015). We evaluate various permeability models, mainly based on MICP measurements, by comparing them to steady-state Darcy flow/permeability measurements. Although for tight rocks typically transient methods (e.g., pulse decay) are used for measuring the permeability, their benefit in terms of receiving more reliable results in shorter time is still a matter of debate (Sander et al. 2017), particularly for rocks with permeabilities $> 10\text{E}-20\text{ m}^2$. The BIB-SEM application enables microstructural investigation of relatively small rock pieces and quantification of pore sizes down to c. 5 nm (Klaver et al. 2012). Additional capillary tube modeling then provides a solid basis for comparison with permeability measurements in tight rocks (Philipp et al. 2017; Sinn et al. 2017).

Geological background

During the Jurassic, the study area was occupied by an epicontinental sea as part of the northern to northwestern Tethys shelf (e.g., Koch et al. 2005; Meyer 1996; Pieńkowski et al. 2008). Stress-induced lithospheric deflections related to far-field compression (Scheck-Wenderoth et al. 2008) and a wrench-dominated tectonic regime at the southern end of the North Sea rift system (Pharaoh et al. 2010) led to rapid shallowing of the South German shelf areas during the latest Jurassic to earliest Cretaceous. This resulted in the deposition of peritidal carbonates and anhydrites, and ultimately led to their exposure and pronounced erosion (Bachmann et al. 1987; Schröder 1968; Vejbæk et al. 2010; Voigt et al. 2007, 2008; Ziegler 1990). Widespread post-Jurassic, Mid- to Late-Cretaceous erosion and karstification due to compressional stresses associated with the reactivation of NW–SE and NNE–SSW striking normal faults (e.g., Peterek et al. 1996; Schröder 1968, 1987; Voigt et al. 2007; Wagner et al. 1997) were followed by a sea-level rise, recorded by a northward marine transgression (Bachmann et al. 1987;

Scheck-Wenderoth et al. 2008). After a phase of tectonic quiescence, N–S to NW–SE oriented far-field compressive stresses within the Central European lithosphere related to the Alpine Orogeny (e.g., Scheck-Wenderoth et al. 2008; Ziegler 1987; Ziegler et al. 1995) and/or the onset of Africa-Iberia-Europe convergence (Kley and Voigt 2008) caused the Late-Cretaceous inversion and the formation of N–S to NNW–SSE trending strike-slip faults accompanied by stylolites with orientations vertical to bedding, bedding parallel, and sub-parallel to the strike of normal faults (Koehler et al. 2022) as well as the reversed reactivation of NW–SE striking normal faults (Zulauf 1993). Ultimately, Late-Cretaceous inversion not only led to a cessation of Cretaceous sedimentation but also to the erosion of several hundreds of meters of Mesozoic sediments and widespread reverse reactivation of normal faults (Bachmann et al. 1987; von Eynatten et al. 2021; Fazlikhani et al. 2022; Scheck-Wenderoth et al. 2008; Voigt et al. 2008, 2021). A second major uplift phase between latest Late Cretaceous and Palaeocene was caused by the combined effects of the Alpine continental collision (Peterek et al. 1997; Reicherter et al. 2008; Schröder 1987; Wagner et al. 1997; Ziegler 1987) and mantle-induced domal uplift in the area of the Upper Rhine Graben Rift (URG) to the west of the study area (von Eynatten et al. 2021) (Fig. 1 inset). Consequently only erosional remnants of Cretaceous and Cenozoic sediments of < 100 m thickness are preserved in the Frankenalb of N Bavaria (Meyer 1996) but significantly higher thicknesses of > 5000 m are preserved within the SGMB to the south of the study area (Bachmann and Müller 1992; Meyer 1996).

A detailed description of limestone facies and petrography in the study area is given by Koch et al. (2005). Lower Kimmeridgian mud- to wackestones are overlying well-bedded Oxfordian limestones, separated by thick marl beds of the Platynota zone (Koch et al. 2005; Meyer 1974; Zeiss 1977). Thick-bedded Middle Kimmeridgian limestones form the top of the section.

Materials and methods

Sampling

To minimize surface weathering effects, our test field is located in an active quarry near the town of Simmelsdorf, about 38 km to the northeast of Nuremberg (Fig. 1), exposing Upper Jurassic (Malm) limestones. Exposed sub-horizontal beds vary in thickness from 0.1 to 0.6 m and were consecutively labeled B-2 to B10 (Fig. 2B and C). A total of 40 carbonate Malm β samples were collected for this study's workflow (Fig. 2A) from a NNE-SSW outcrop section (Fig. 2B and C), which is oriented sub-perpendicular to two NW–SE trending normal faults forming a graben structure. The offset of the normal faults is relatively small, approximately 0.5 m. Blocks (~ 50 cm × 50 cm × 40 cm) of each bed (Fig. 2B and C) were systematically sampled in a vertical section at approximately six meters distance to the fault and numbered 0 to 10. For a horizontal section, blocks of similar size were extracted from bed B1 every few meters and labeled 1E–H (Fig. 2B) and 1A–D (Fig. 2C). The blocks were carefully removed by an excavator, layer by layer. They were cut on-site into smaller pieces and a selection of samples from the vertical section was drilled with diameters of c. 6 cm and 3 cm to get cores (6 × 20 cm) and plugs (3 × 4 cm) suitable for further lab-based Multi-Sensor Core Logger (MSCL), gas permeability (plugs), helium

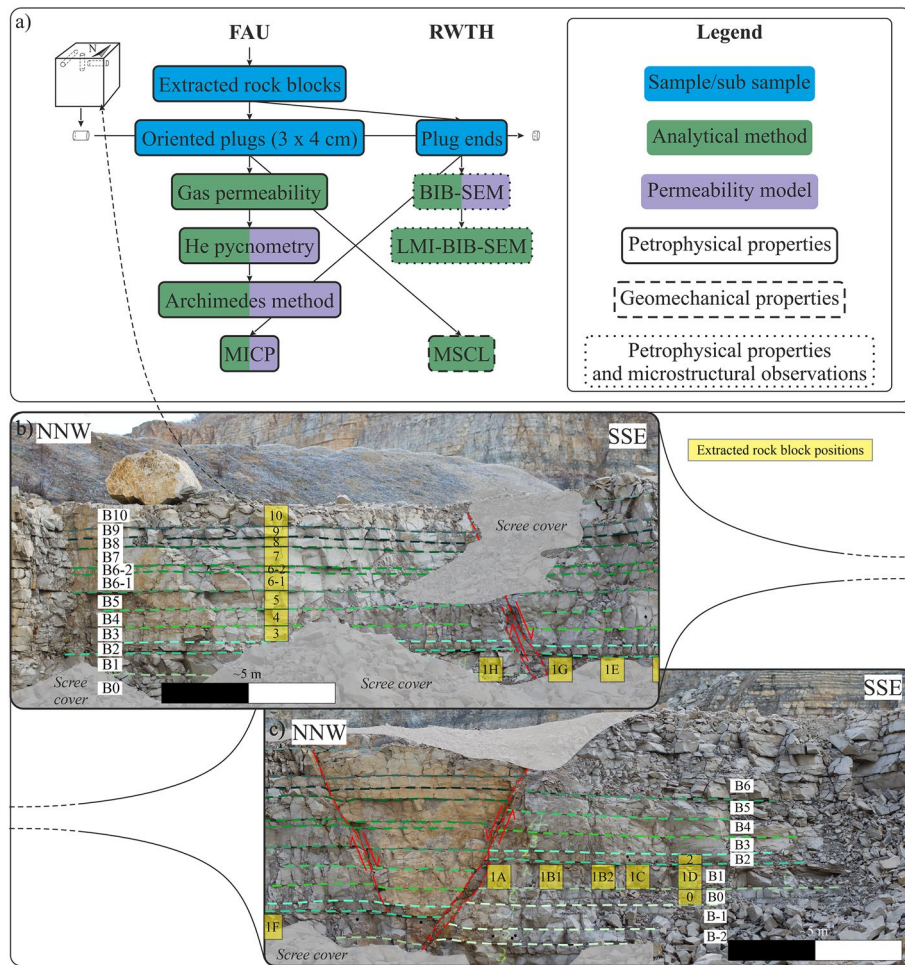


Fig. 2 **A** Workflow from sampling to analysis and data usage; **B** and **C** are photos of the exposed quarry walls (see Fig. 1 for quarry location) illustrating consecutive labeling of beds B-2 to B10 (white background) and positions of the sampled rock blocks (yellow background), labeled 0 to 10 (vertical sampling) and 1A to 1H. (horizontal sampling of B1). Traces of NW–SE striking normal faults and inferred polarity of offset in red

pycnometry (plugs), and BIB-SEM analyses (sub-samples of plug ends). Cores were always drilled from the non-fractured part of the blocks to avoid disintegration.

Visual inspections of sampled blocks and cores were carried out as a preliminary analysis to identify local lithological heterogeneities and to provide guidance on where to sub-sample the cylinder-shaped plugs for the petrophysical measurements and further BIB-SEM investigations. The presence and the orientation of stylolites were noted for each plug. Additional 40 plugs and sub-samples were taken from all samples of both, the vertical as well as the horizontal sections for gas permeability (plugs) and supplementary MICP measurements (sub-samples). All plug samples were dried in an oven at 105 °C until weight constancy was reached over a period of 24 h before any kind of analysis was performed.

Microstructural investigations via BIB-SEM

The plug ends of each sample from the vertical section were sub-sampled for microstructural analyses using BIB-SEM. The 5 sub-samples have maximum dimensions of $4 \times 10 \times 6 \text{ mm}^3$ (height \times width \times depth) and were taken from a macroscale relatively homogenous, representative part of the plug ends. The BIB cross-section was polished using the JEOL SM-09010 cross-section polisher producing a 1 mm^2 planar Gaussian-shaped cross-section on the sample by removing approximately $100 \text{ }\mu\text{m}$ of material in 8 h (Klaver et al. 2012). Prior to SEM image mapping by a Zeiss Supra 55 Field Emission SEM, samples were prepared with approximately 7.5 nm of tungsten coating. In the SEM, the pore space was imaged with the secondary electron (SE2) detector systematically in a raster pattern throughout the whole BIB section at about 50 locations without overlap. At each location 5 images were acquired with different magnifications of 2500, 5000, 10,000, 20,000, and 40,000 times. This approach enables unbiased sampling of the whole section and scans a wide range of pore sizes simultaneously. The visible BIB-SEM porosity was quantified by calculating the fraction of visible pore space using image segmentation (Klaver et al. 2012) for 5 selected cross-sections on several single images. The other BIB cross-sections were used for qualitative investigations as the pore microstructures were similar to each other according to visual inspection.

Two additional sub-samples were injected with Wood's Metal (LMI-BIB-SEM) following the workflow of Klaver et al. (2015) at 100 and 200 MPa, respectively. As Wood's Metal has non-wetting properties comparable to mercury, it is a similar principle as MICP, though the Wood's Metal is solid at room temperature, which enables visualizing the metal-filled pore space. Subsequently, after BIB low angle polishing in a Leica TIC3X BIB, the metal-filled pore space was imaged in the SEM to qualitatively evaluate the pore connectivity in the carbonate matrix.

Petrophysical methods

Porosity

Multi-Sensor Core Logger (MSCL) The Geotek Multi-Sensor Core Logger (MSCL) system includes an assembly of tools that log the geophysical and geochemical properties of cores. For this study, only data acquired by the gamma density tool were used, and a total of 0.94 m core lengths were measured at 1 cm intervals. The samples were exposed to a focused beam of gamma rays (energies principally at 0.662 MeV) that become attenuated by Compton scattering while they pass through the core with the degree of attenuation directly relating to the diameter and the electron density of the core. The bulk density (ρ_{bulk}) of the measured core section was then calculated by measuring the number of transmitted gamma photons that passed through the core unattenuated (I), considering the core thickness (d):

$$\rho_{\text{bulk}} = \frac{1}{\mu d} \ln \frac{I_0}{I} \times 100, \quad (1)$$

where μ is the Compton attenuation coefficient and I_0 the gamma source intensity (Weber 1997). The porosity Φ_{GD} (%), in the following termed gamma ray (GD) porosity,

is calculated by applying gamma ray-derived bulk density (ρ_{bulk} , g/cm³), matrix density ($\rho_{\text{matrix}} = 2.71$ g/cm³ for CaCO₃), and the density of air ($\rho_{\text{Air}} = 0.001225$ g/cm³):

$$\Phi = \frac{\rho_{\text{matrix}} - \rho_{\text{bulk}}}{\rho_{\text{matrix}} - \rho_{\text{air}}} \times 100. \quad (2)$$

Archimedes (buoyancy) isopropanol immersion method The Archimedes method was applied to a total of 40 drilled cylindrical core plugs. Advantages, disadvantages, operating principle, and potential measurement errors of the method are thoroughly discussed by Hall and Hamilton (2016). The Archimedes porosity Φ (%) was calculated via Eq. 3:

$$\Phi = \frac{V_p}{V_{\text{tot}}} \times 100 = \frac{m_{\text{sat}} - m_{\text{dry}}}{m_{\text{sat}} - m_{\text{im}}} \times 100, \quad (3)$$

where V_p (m³) is the open pore space volume filled with isopropanol, derived from subtracting the dry mass m_{dry} (g) from the saturated mass m_{sat} (g). Saturating the open pore space with isopropanol was achieved by fully submerging the sample in an isopropanol bath and placing it in a vacuum chamber until no visible air bubbles were exiting the sample. V_{tot} (m³) is the total volume of the sample, including the open pore space and the solid rock matrix volume, which is equal to the difference between the saturated mass m_{sat} and the weight m_{im} (g) of the sample submerged in isopropanol. The weights were determined by a Sartorius ED2245 working at an accuracy of 0.1 mg. Only open pores that are connected to the open pore network of the sample are determined by this method, as the isopropanol cannot access closed pores (Zinszner and Pellerin 2007).

He pycnometry Helium porosity measurements were carried out on 40 selected plugs from the horizontal and vertical sections. The porosities were calculated based on the difference between the total dry plug volume (calculated from diameter and length measures by a high precision gauge) and the matrix volumes determined by a Micromeritics AccuPyc 1330 pycnometer. The instrument measures the skeletal volume of a sample at an accuracy of 0.03% (i.e., matrix volume) by the gas displacement technique, based on the ideal gas law. The use of helium gas enables the filling of connected pores as small as 0.1 nm in diameter.

Mercury injection capillary pressure (MICP) Mercury intrusion porosimetry is one of the most widely used methods to determine the bulk porosity and the pore (throat) size distribution by utilizing the property of non-wetting liquids that only intrude capillaries under pressure. Washburn (1921) described this relationship between pressure and capillary diameter:

$$P = \frac{-4\gamma \cos \theta}{d_{\text{cap}}}, \quad (4)$$

where P is the pressure (Pa), γ the surface tension of the liquid (in this case mercury) (mN/m), θ the contact angle of the liquid (for mercury $\theta = 140^\circ$), and d_{cap} the diameter of the capillary (m). The intruded volume of mercury entering the pores at each pressure increment is recorded and from that, the pore (throat) size distribution is derived,

whereas the total porosity can be calculated from the total intruded mercury volume (Abell et al. 1999). The r_{35} values correspond to the pore diameter (μm) at 35% mercury saturation, while r_{Main} (μm) gives the pore diameter at which the largest amount of mercury intruded, with both values listed in Appendix 1: Table 4. We used the PoreMaster 60 by Quantachrome, operating at an accuracy of $\pm 1\%$ fso (full Scale Output) of sample cell stem volume on 24 samples.

Permeability measurements

Permeability k_{Ar} measurements (in m^2) were carried out on 12 samples, using argon gas. The 1-inch diameter plugs were placed inside a stainless-steel cylinder (autoclave) and permeability determinations were carried out at increasing gas pressure steps of 1 bar with a confining pressure P_{conf} of 15 bar. For each plug, the flow rate through the sample was measured at six different injection pressure steps P_{inj} , from 3 to 8 bar to correct for the so-called “Klinkenberg Effect” (Klinkenberg 1941). After each pressure increment, the flow was measured once measurements were stable for at least ten minutes before proceeding to the next step.

A similar method was applied to determine the permeability (k_{Air}) of all samples (34), using compressed air instead of argon. Once a stable flow after a minimum of 10 min was established at a particular pressure increment, the gas (air) flow rate exiting the sample was measured every second over a period of 30 s. An “Aarberg” mass flow meter operating at an accuracy of 1% at flow rates between 0 to 50 ml/min was used as logging device. Due to mechanical limitations, only a confining pressure of 8 bar could be applied. Therefore, the maximum flow rate through the sample was reached at a pressure of 5.8 bar, before the through-flowing air might have bypassed the sample due to a too low difference between confining and injection pressure. A Klinkenberg correction for the permeability measurements with air was not possible, as we received negative slip-page factors. Possible reasons for that are discussed later. We, therefore, also used the uncorrected, mean measured permeabilities for the comparison to other applied methods and models.

Permeability models

Many different permeability models that were calibrated or validated on different sample sets over the last decades were applied to our data set but only the permeability estimation models that performed best will be treated and discussed in this study.

Models based on percolation theory

Permeability estimation based on MICP data was introduced by Katz and Thompson (1986, 1987). Their model is based on the percolation theory (K–T Model) and relates the pore diameter l (m) to the intrinsic permeability k_{KT} (m^2). When l is optimally selected, k_{KT} (m^2) can be derived via Eq. (5):

$$k_{KT} = \frac{1}{89} \Phi \frac{(l_{max}^h)^3}{l_c} f(l_{max}^h) \times 100, \quad (5)$$

where Φ (%) represents the porosity of the rock, l_c (m) the critical length, l_{max}^h (m) the maximum hydraulic length, and $f(l_{max}^h)$ the fraction of the whole rock that is filled by mercury at l_{max}^h . While critical length l_c is defined as the critical pore diameter at which mercury can finally percolate through the sample (equal to the steepest slope of the capillary pressure vs. cumulative porosity curve after cut-off), l_{max}^h corresponds to the capillary pressure, where the product of the mercury saturation and the cubic pore throat diameter, $f(l_{max}^h) * l^3$, are at its maximum (Nishiyama and Yokoyama 2014; Rashid et al. 2015). Originally, the theoretical consideration that the pore's diameter is equal to its length led to the constant 1/89 (Nishiyama and Yokoyama 2014; Rashid et al. 2015). However, this constant was empirically determined for porous rocks. As this study focuses entirely on tight carbonates, a value of 1013/89 for C was used instead, based on the work of Rashid et al. (2015) recommending this value for tight carbonates.

Poiseuille-based models

RASHID et al. (2015) apply eight permeability models, all based on the Poiseuille Model. We tested a selection of these models, too. The Winland Model was originally introduced in various unpublished reports between 1972 and 1976, which we could not obtain; we therefore reference published studies by Comisky et al. (2007), Gunter et al. (2014), and Rashid et al. (2015). The Winland Model uses the radius r_{35} (μm), which is calculated using the Washburn equation (Eq. 4) at a mercury saturation of 35% (Rashid et al. 2017) and relates it to permeability k_w (in m^2) according to

$$k_w = C_w \times r_{35}^{a_1} \times \Phi^{a_2} \times cf, \tag{6}$$

where C_w , a_1 , and a_2 are empirically determined variables (-), Φ is the porosity (%), and cf ($= 9.86923 \times 10^{-16}$) is the factor for converting milliDarcy (mD) to m^2 . These variables were derived from the calibration of Winland's equation on a data set consisting of 82 samples, 56 of which were sandstones and 26 carbonates (Klinkenberg-corrected permeabilities), as well as 240 samples, where only uncorrected air permeabilities were known. The calibration resulted in the following values: $C = 49.4$, $a_1 = 1.70$, and $a_2 = 1.47$.

Dastidar et al. (2007) introduced another Poiseuille-based permeability model (Dastidar Model), calibrated on tight gas sandstones. The authors suggest taking the entire pore throat spectrum into account when estimating the permeability from MICP data. They introduced a length scale based on the geometric mean of the pore throat radius (r_{wgm}) which is calculated:

$$r_{wgm} = \left[\prod_{i=1}^n R_i^{w_i} \right]^{\frac{1}{\sum_{i=1}^n w_i}}, \tag{7}$$

with the pore throat radius R_i at the i th capillary pressure (m), the total number of incremental pressure steps n , and w_i the ratio of the incremental mercury volume intruded into the sample at the specific capillary pressure p_i (Pa) and the total mercury volume intruded (m^3). With this, we can calculate permeability k_D (in m^2) after Dastidar et al. (2007), where cf is the factor for converting mD to m^2 :

$$k_D = 4073 \times r_{\text{wgm}}^{1.64} \times \Phi^{3.06} \times cf. \quad (8)$$

An alternative Poiseuille-based model is the CT Model (or CTM) that can be directly applied to the pore geometries determined from segmented BIB-SEM images. It assumes that the flow through the rock is analog to laminar flow through a bundle of pipes. As pore networks in rocks are never perfectly straight round tubes, but follow a tortuous path, a modified version of the Hagen–Poiseuille equation, taking into account the tortuosity factor τ (–) (Philipp et al. 2017; Sinn et al. 2017), is employed to determine permeability k_{H-P} (in m^2) according to the CT Model:

$$k_{H-P} = \frac{1}{8} \sum_{i=1}^n \frac{r_i^2 \Phi_i}{\tau^2} * cf, \quad (9)$$

where r_i (m) equals the hydraulic radius (pore area divided by its perimeter), Φ_i is the porosity (%) of each segmented pore in the BIB-SEM image, and cf is the factor for converting mD to m^2 . The tortuosity value can be a fitting parameter or taken from literature data. For this study, a tortuosity of 2.0 was assumed initially, as tight carbonates are slightly less tortuous than tight sandstones (Cai et al. 2019) with typical values of 2.1 (Du 2019).

The Kozeny-Carman Model (K–C Model) is an extension by Carman (1937) that bases on the permeability model developed by Kozeny (1927). He used the specific surface area related to the rock volume S_0 (1/m) and the effective porosity Φ_{eff} (%), hence the pore space contributing to fluid flow (Fens 2000):

$$k_{K-C} = c\tau^2 \frac{\Phi_{\text{eff}}^3}{S_0^2(1 - \Phi_{\text{eff}})^2} * cf, \quad (10)$$

with the Kozeny constant c and τ as the tortuosity factor, the permeability k_{K-C} (m^2), based on the K-C Model), and cf the factor for converting mD to m^2 . S_0 was obtained from MICP data. The tortuosity factor τ is derived from the optimized CT Model and the Kozeny constant c for cylindrical capillaries is 1.57 (Carman 1937).

Empirical models

Although various empirical equations exist, we only applied the models developed by Bohnsack et al. (2020), Saki et al. (2020), Lucia (2001), and Jennings and Lucia (2003) in this study.

Based on the porosity–permeability relationship measured on a subset of ~50 mud-supported limestones out of a set of 363 Upper Jurassic limestone core samples, Bohnsack et al. (2020) inferred the following power law (termed Bohnsack Model)

$$k_B = 2.0E^{-04} \times \Phi^{3.10} \times cf, \quad (11)$$

where k_B is the permeability (m^2), Φ the effective water porosity (%), and cf the factor for converting mD to m^2 .

Saki et al. (2020), on the other hand, established the following relationship (termed Saki Model) between gas permeability, porosity, and pore/throat diameters from 187

sandstone, limestone, and dolostone samples derived from 8 different Iranian oil and gas fields:

$$k_S = \exp(0.0583 + 1.4660 \times \log r_{35} + 0.6993 \times \log \Phi) \times cf, \tag{12}$$

where k_S is the gas permeability (m^2), Φ the porosity (%), r_{35} is the smallest pore throat radius (μm) filled by mercury at 35% mercury saturation, and cf is the factor for converting mD to m^2 .

An extensive study on a variety of limestones ($n=416$) was conducted by Lucia (2001) and Jennings and Lucia (2003). They related rock-fabric petrophysical classes and inter-particle porosity to permeability via a multilinear regression, termed global porosity–permeability transform (GPPT). Each rock-fabric petrophysical class represents a different type of pore distribution and interconnection (Lucia 1995). Three classes are thereby distinguished and assigned a specific *rock-fabric number* (rfn) (0.5–4.0): class 1 represents grainstones and coarse-crystalline dolostones with an rfn of 0.5–1.5, class 2 includes grain-supported packstones and medium-crystalline dolostones with an rfn between 1.5 and 2.5, and class 3 comprises mud-supported limestones and fine-crystalline dolostones with an rfn of 3.5–4.0 (Lucia 2001). The GPPT Model is given by

$$k_{GPPT} = \exp((A - B \times \log(rfn)) + (C - D \times \log(rfn)) \times \log(\Phi_{ip})) \times cf, \tag{13}$$

where k_{GPPT} is the rock permeability (in m^2) based on Lucia (2001) and Jennings and Lucia (2003), $A=9.7982$, $B=12.0838$, $C=8.6711$, $D=8.2965$, Φ_{ip} the fractional inter-particle porosity (effective porosity), and cf the factor for converting mD to m^2 .

Geomechanical properties

Geomechanical parameters, such as the dynamic Poisson’s number ν^{dyn} (–), dynamic Young’s Modulus E^{dyn} (GPa), the dynamic Bulk Modulus K^{dyn} (GPa), and the dynamic Shear Modulus G^{dyn} (GPa), are calculated from P- (V_p) and S-wave (V_s) velocities (m/s) which were measured on 33 limestone samples using an automated core logger equipped with a Geotron.UKS12 ultrasonic device. This comprises conical-shaped piézolectric stainless-steel p-wave transmitter and receiver probes, operating with pulse transmission at a frequency of 80 kHz and measuring the time taken by the first p-wave to cross the sample. Only plugs that were drilled vertically to bedding were measured. For each sample, five measurements were conducted for reproducibility reasons. For a detailed description of the operating principle of the ultrasonic core logging device we refer to the study of Filomena and Stollhofen (2011). The dynamic geomechanical parameters were derived from the following equations (Schön 2015):

$$\nu^{dyn} = \left(0.5 \times V_p^2 - V_s^2\right) \times \left(V_p^2 - V_s^2\right)^{-1}, \tag{14}$$

$$E^{dyn} = ((1 + \nu) \times (1 - 2\nu)/(1 - \nu)) \times V_p^2 \times m_{dry}/V_{Ges}, \tag{15}$$

$$K^{dyn} = E/(3 - 6 \times \nu) = -dp/dV/V > 0, \tag{16}$$

$$G^{\text{dyn}} = E/2 \times (1 + \nu). \quad (17)$$

A detailed description of the derivation of the relative porosity change $\Delta\Phi$ (%) with increasing depth, hence effective pressure P_e (Pa), is given by Bohnsack et al. (2021) and can be calculated after Cheng (2016) as follows:

$$\Delta\Phi = \frac{\Phi}{\Phi_i} = e^{-3P_e/4G^{\text{dyn}/\text{stat}}}, \quad (18)$$

with Φ_i representing the initial porosity (%), measured with the Archimedes method. However, from Cheng (2016) it does not emerge whether he refers to the dynamic (G^{dyn}) or the static (G^{stat}) shear modulus. Therefore, we calculated the relative porosity change for both shear moduli. As the static shear modulus cannot easily be calculated from the dynamic shear modulus, we used the empirical correlation by Bastos et al. (1998) for limestone samples:

$$G^{\text{stat}} = 0.621 \times G^{\text{dyn}} - 0.95. \quad (19)$$

Further models were introduced by Bohnsack et al. (2021) and Hu et al. (2020), applying solely porosity stress sensitivity coefficients that were adjusted to the specific data set and the differential pressure $P_e - P_i$ (atmospheric pressure). As the stress sensitivity values were not available for our data set, we did not include these relationships in our study.

The relative change in permeability Δk with increasing effective stress can be calculated from various equations, integrating different empirically determined parameters. Applying β as dimensionless constant for the stress sensitivity exponent, provides the following exponential law (Bohnsack et al. 2021; David et al. 1994; Xu et al. 2018a, b):

$$\Delta k = \frac{k}{k_i} = e^{-\frac{3\beta P_e}{4G^{\text{dyn}/\text{stat}}}}. \quad (20)$$

For β , β_{Min} (= 28.3) and β_{Max} (= 46.3) values were determined by Bohnsack et al. (2021) for limestones of the Upper Jurassic (Malm Zeta) from two drill cores in the SGMB that were subsequently used to calculate Δk_{Min} and Δk_{Max} , respectively. Again, two further models by Shi and Wang (1986) and Katsube et al. (1991) describe the relative permeability change with increasing effective stress, solely applying stress sensitivity-describing parameters adjusted to the specific data set and the differential pressure $P_e - P_i$. As the stress sensitivity parameters were also not available in this study, we excluded these models from our study.

Results

The investigated Oxfordian to Lower Kimmeridgian limestones classify as mud- to wackestones (Cohen et al. 2013; Koch et al. 2005) and can be described as mud-supported limestones, organized in horizontally layered, continuous beds (Fig. 2) which only rarely contain fossil remnants or vugs filled with pyrite. These beds are separated by thin marlstone layers. The alternating lime-marlstone layers are crosscut by three normal faults, each of which showing an offset of ~ 2 m. In general, these limestones are fine-grained and have a very homogeneous appearance. Only rarely they are bearing fossil

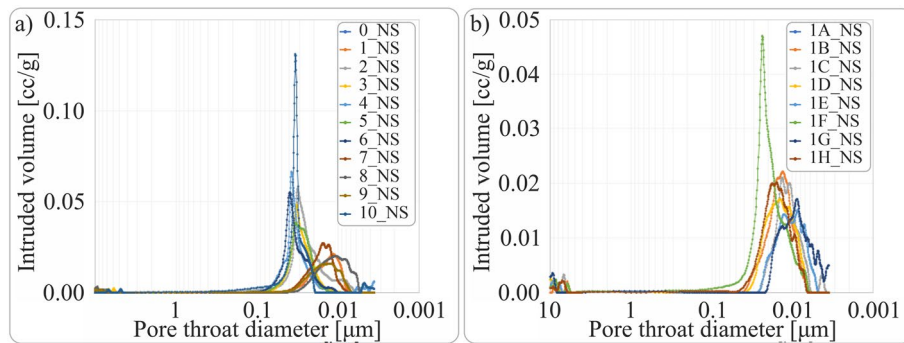


Fig. 3 MICP results showing the pore throat size distributions as intruded volume [cc/g] versus equivalent pore throat diameter of the **a** vertical section, and **b** horizontal section

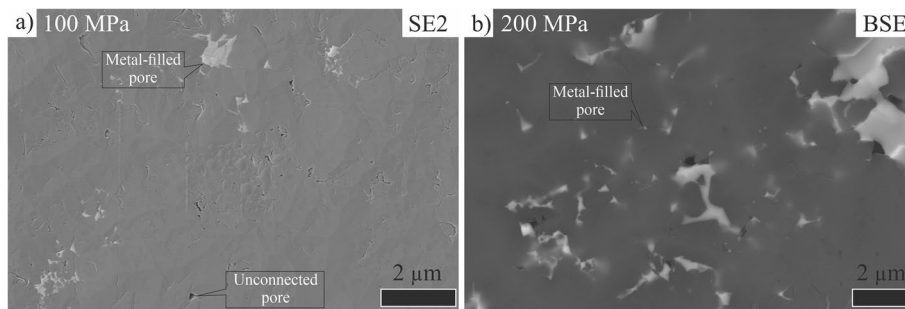


Fig. 4 LMI-BIB-SEM result of injected sub-samples at **a** 100 MPa and **b** 200 MPa indicating that only at 200 MPa virtually all visible interparticle pores were filled with Wood's metal (bright gray)

remnants and occasionally horizontal, oblique, and vertical pressure solution seams or stylolites are developed with increasing frequency toward the faults.

Pore throat sizes and pore connectivity

A summary of all petrophysical measurement results is listed in Appendix 1: Table 3, Table 4, and Appendix 1: Table 5. In total, 24 samples were analyzed using MICP. The results for the vertical section (Fig. 3A) show a unimodal pore diameter distribution for most samples. The samples 0, 1, 7, 8, and 9 have pore throat diameters of around 11–15 nm, and samples 2, 3, 4, 5, 6, and 10 had larger pore throats, with diameters of 31–39 μm . The pore throat size distribution of most samples from the horizontal section are clearly conform to each other (Fig. 3b). All samples had pore throat diameters of 9–15 nm, except sample 1F which had slightly larger pore throat diameters averaging 23 nm. However, some samples (1G, 4, and 10) indicate continued mercury intrusion even at the device's maximum pressure, corresponding to the smallest pore diameter of 3 nm (Fig. 3). All samples were conformance corrected ($> 4 \mu\text{m}$) for surface irregularities (Newsham et al. 2004; Sigal 2009). In conclusion, the samples are relatively homogeneous and reflect a narrow pore throat size distribution with small variations between 8 and 40 nm and no trends related to fault proximity or bed thicknesses (see Fig. 1b for corresponding sample positions relative to the fault).

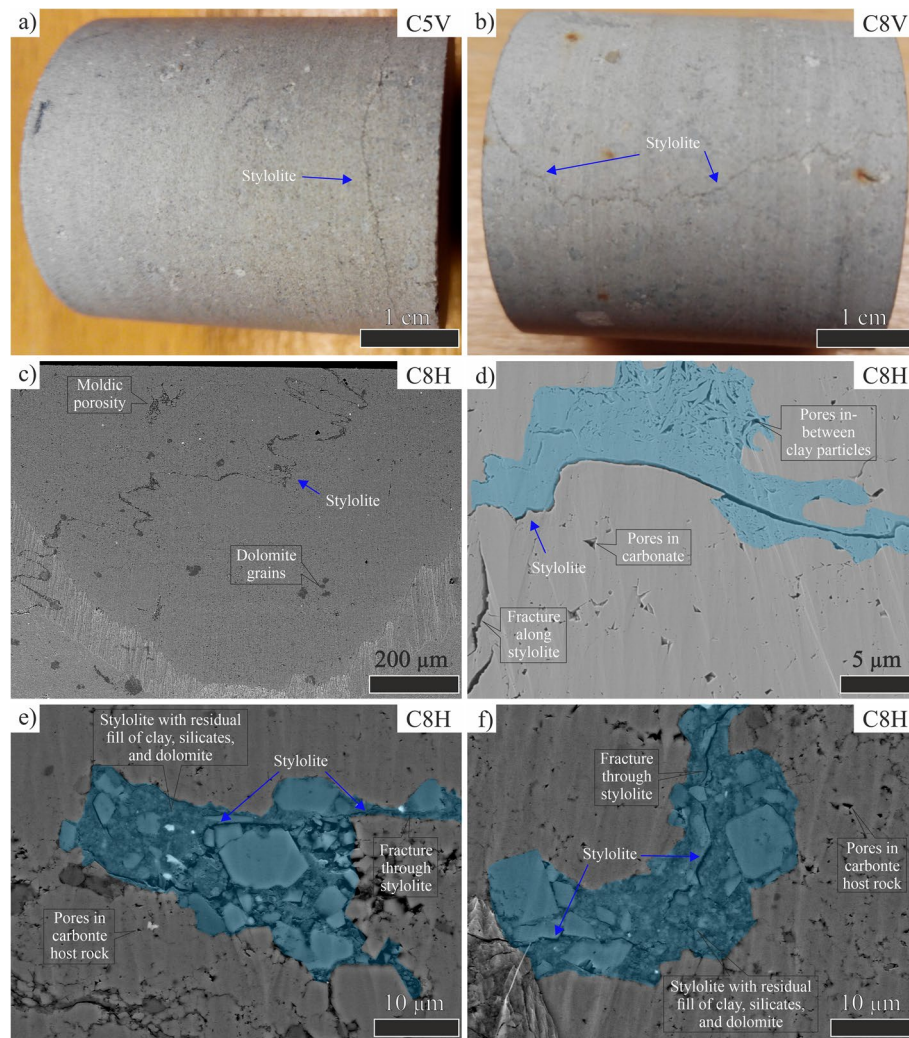


Fig. 5 Examples of typical microstructures in analyzed limestone samples with **a** and **b** showing stylolite planes (highlighted by blue dashed lines) in core plugs, **c** SE2 image of stylolite plane in BIB section, **d** stylolite plane and interparticle pores in clay, and **e** and **f** BIB-SEM images showing the fracture through the stylolite with residual fill of clays, silicates, and dolomite grains containing interparticle and intercrystalline submicron scale porosity, see text for further details

The MICP breakthrough fits well with BIB-SEM observations on the Wood's Metal injected (LMI-BIB-SEM) samples at 100 and 200 MPa, equivalent to pore throat diameters of approximately 15 and 9 nm (Fig. 4). The sample injected at lower pressure (100 MPa) showed both filled and unfilled interparticle pores (Fig. 4A), indicating a percolating network that was not fully reached by the injection at this low pressure. Instead, the samples injected at twice the pressure (200 MPa) showed that virtually all visible interparticle pores were filled with metal (Fig. 4B).

Microstructure and pore geometry

All plugs prepared for the gas (Ar) permeability tests were macroscopically investigated regarding the presence and orientation of stylolites (Appendix 1: Table 3*). A quarter of

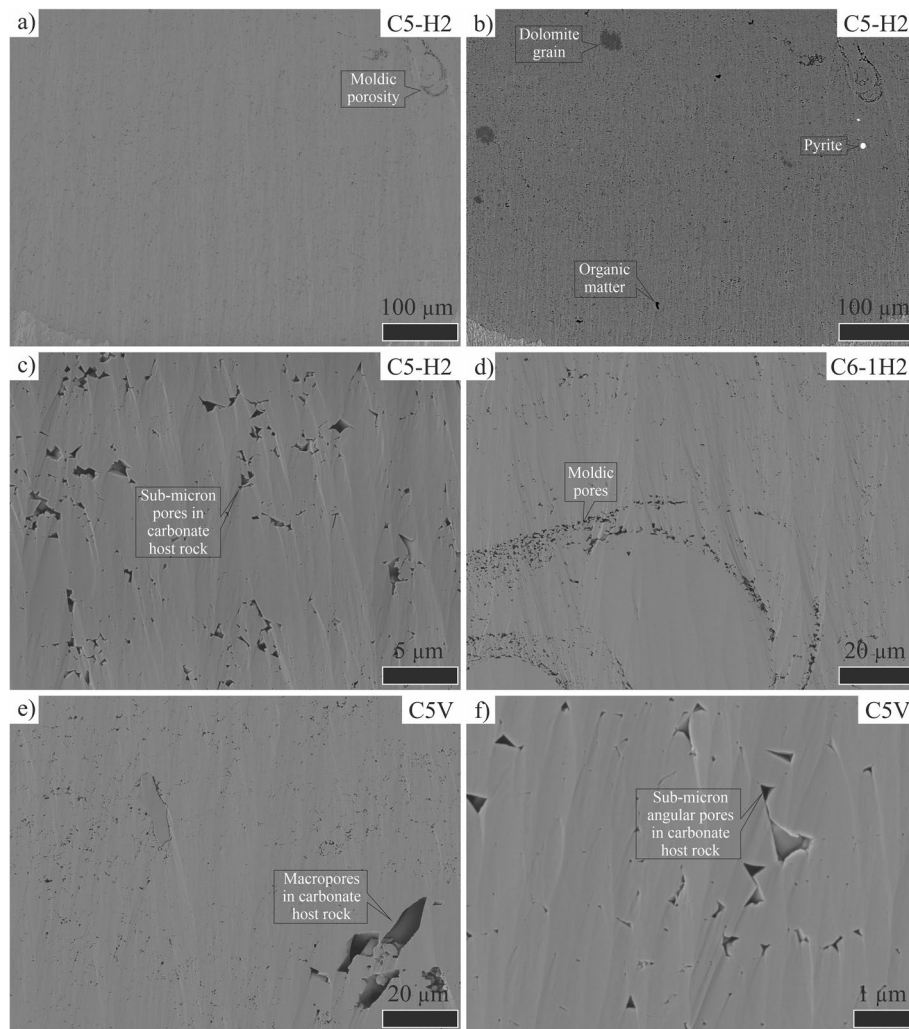


Fig. 6 Typical microstructures identified in the investigated limestone samples. **a** SE2 image of the BIB cross-section at low resolution (pixel size 800 nm) indicating low visible porosity and moldic porosity associated with a foraminifera. **b** BSE image of **a** illustrating homogeneous mineralogy with only a few dolomite grains, pyrite, and organic matter particles. **c**, **d** SE2 overview images of visible porosity at high resolution (pixel size: **c** 29 nm; **d** 117 nm) indicating the submicron scale of the pore sizes. **e** SE2 image displaying one of the relatively few macropores detected in the BIB cross-sections. **f** High-resolution SE2 image of the typical angular pore geometries in the carbonate host rock

the plugs contained stylolites identifiable at macroscale, both sub-parallel to the bedding (Fig. 5A) as well as sub-perpendicular to bedding (Fig. 5B). Such pervasive stylolites were clearly visible in the SEM and were examined at very high detail in the BIB cross-section to determine and characterize different types of microporosity (pores < 1 micron) and nanoporosity (pores < 100 nm) (Fig. 5C–F).

Figure 5D illustrates the presence of nanoporosity along the stylolite plane in contrast to the almost tight nature of the limestone's matrix containing only few clusters of interparticle nanopores. Insoluble minerals, like clay, quartz, dolomite, and denser minerals, accumulated as solution residues at the stylolites' peak tops contributing to interparticle/intercrystalline nano-/microporosity.

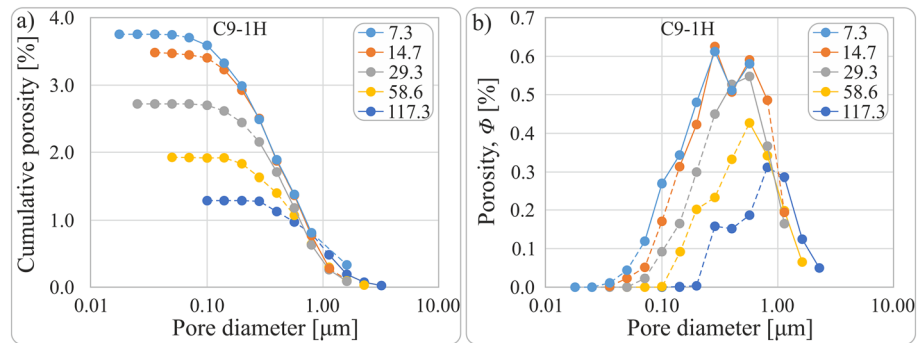


Fig. 7 Typical BIB-SEM pore size and porosity distributions of quantitatively investigated samples. **a** Cumulative porosity versus equivalent circular pore diameter for sample C9-1H. The dashed lines are below the practical pore resolution (PPR) and the color legend corresponds to the pixel sizes related to the 2500 \times , 5000 \times , 10,000 \times , 20,000 \times , and 40,000 \times magnifications used. **b** Porosity vs equivalent circular pore diameter for the example of sample C9-1H at different magnifications distinguished by color

(Fig. 5E and F). Examples of the typical microstructure of the thirteen investigated BIB sections and the resolution dependency of their visibility are illustrated in Fig. 6, showing at low resolution a completely tight matrix (Fig. 6A) or a low porous matrix (Fig. 6B), but at higher resolution a matrix with clusters of moldic pores (Fig. 6C), and nanoporosity associated with larger fossil remnants (Fig. 6D). Besides the moldic pores, the matrix also contains interparticle pores, both being usually smaller than 1 micron (Fig. 6C and D). However, these pores that are associated with partly dissolved fossil remnants and which are recognizable by their specific pore arrangement resembling the shape of fossils are not common in the investigated BIB cross-sections (Fig. 6D). The BIB cross-sections of C5V and C6-2 V (Appendix 1: Table 3) also contain some much larger interparticle (macro)pores (e.g., Figure 6E) which significantly contribute to the visible porosity. In general, very few but spatially distant macropores were observed. Figure 6F shows the typical microstructure at high resolution showing typical (tri-) angular interparticle and intercrystalline pores relatively close to each other. The smallest visible pores that could be segmented are a few pixels in size.

Overall, the average matrix is characterized by pores mostly in the 100 to 1000 nm pore size range in BIB-SEM (Fig. 7A) indicating a general increase of visible nano- and microporosity with improved magnification. However, this increase stagnates at higher magnification, suggesting that not much additional nanoporosity becomes visible beyond 40,000 \times magnification (pixel size 7.3 nm), or below the practical pore resolution (PPR). This is also validated by uniform pore diameter distributions (Fig. 7B), independent from the applied magnification. For the permeability estimation via the CT Model, the measurements at 14.7 magnification (equal to 20,000 \times) were applied to improve pore detection.

Porosity

The MSCL-logged cores show gamma density porosities varying between 3.7 and 5.9% (mean $5.0 \pm 0.7\%$) that are, on average, slightly higher than porosities derived from He pycnometry, ranging from 2.5 to 6.0% (mean $4.3 \pm 1.0\%$) (Fig. 8A and B). The average Archimedes porosities of the different limestone beds in the vertical section range from

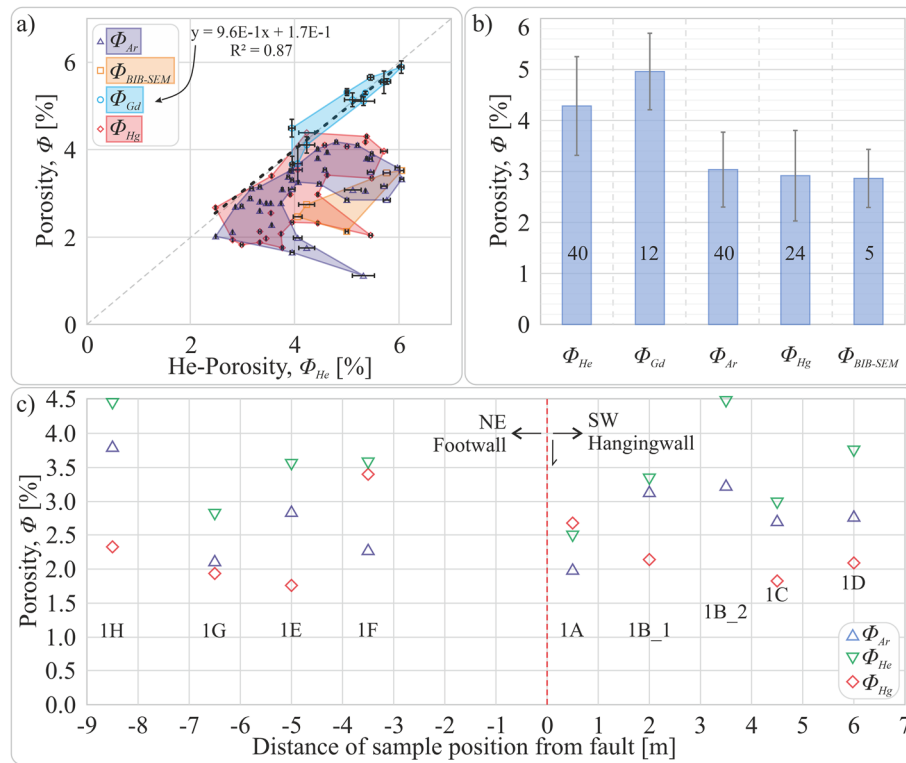


Fig. 8 Porosity diagrams. **a** Archimedes (Φ_{Ar}), BIB-SEM ($\Phi_{BIB-SEM}$), GD (Φ_{Gd}), and MICP porosities (Φ_{Hg}) vs. He porosities (Φ_{He}) derived from vertical section sampling including error bars (standard deviation) if available and method-specific contour lines in the background for better visibility. **b** Comparison of porosity distributions determined by different methods, including error bars (standard deviation) and number of measurements. **c** Φ_{He} , Φ_{Ar} , and Φ_{Hg} porosity evolution with varying distances from the fault (red dashed line). See Fig. 2B for sample positions in c

1.1 to 4.2% (Fig. 8A, B and Appendix 1: Table 3), with an overall average of $3.0 \pm 0.7\%$. Similar ranges and mean porosities were determined by both, the BIB-SEM and MICP methods.

The reported porosities of all applied methods are derived from the vertical section. Complementary Φ_{Ar} , Φ_{He} , and Φ_{Hg} porosities from the same beds and within the horizontal section showed comparable porosity variability and no trend toward increased or decreased porosities with distance from the fault (Fig. 8C). Hence, we conclude that the bulk matrix porosity is almost homogeneous with an average MICP porosity of 2.9% (1.8 to 4.4%). The visible BIB-SEM porosities $\Phi_{BIB-SEM}$ are also on average 2.9%, varying from 2.1% to 3.5%. Macropores are present; however, they are rather distant from each other in the tight matrix so do not affect the fluid transport properties significantly. Additionally, (micro-) fractures were purposely excluded from the BIB-SEM analyses as our focus was on the microporosity of the matrix.

Permeability and permeability models

The measured air permeabilities K_{Air} vary between $1.9E-18 \text{ m}^2$ and $10.8E-18 \text{ m}^2$ with a mean of $6.8E-18 \pm 2.1E-18 \text{ m}^2$. The lowest determined permeability equals the detection limit of the device, at least for air injection pressures up to ~ 6.8 bar. A mean of 1.4

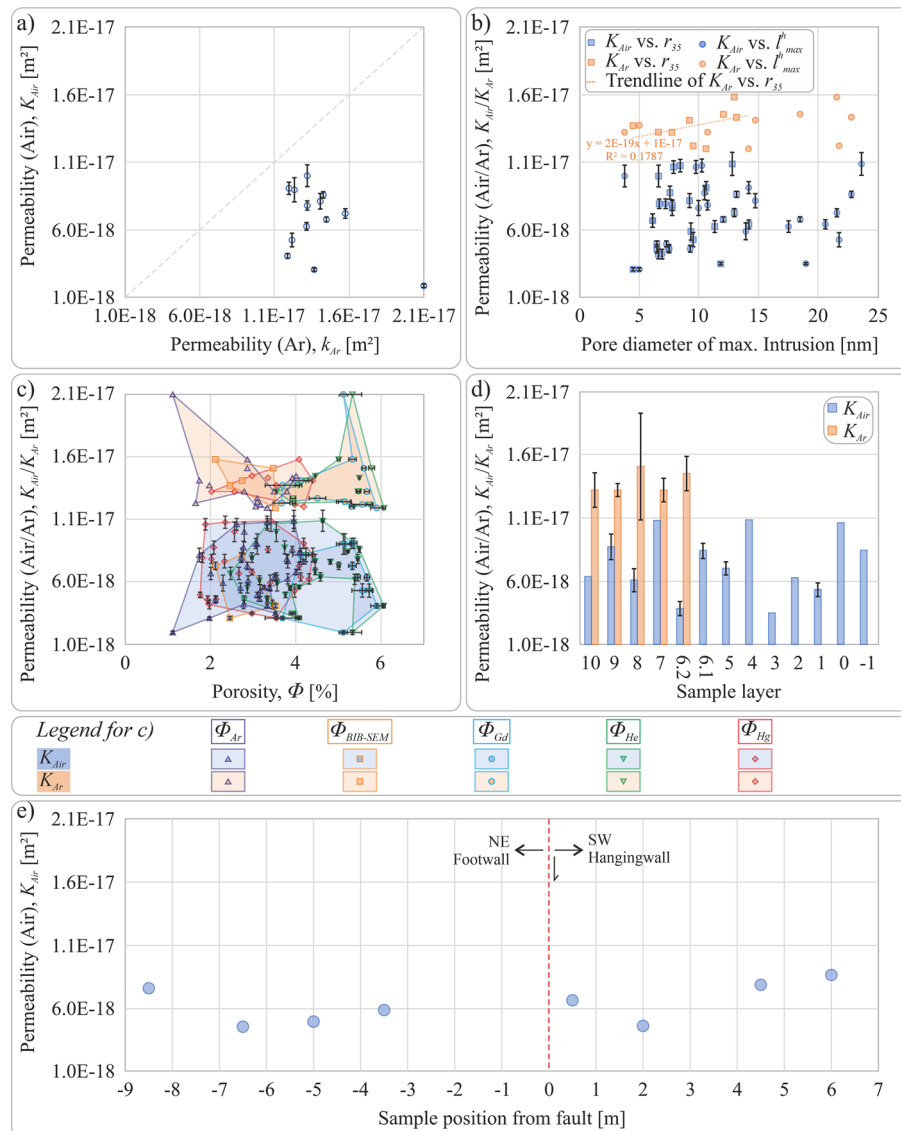


Fig. 9 **a** Correlation between permeability values determined by argon and air measurements, including error bars (standard deviation) if available, **b** permeabilities measured with argon (K_{Ar}) and air (K_{Air}) plotted against the corresponding maximum hydraulic length l_{max}^h (m), where most of the mercury is injected into the sample as well as the r_{35} value, corresponding to the pore diameter at 35% mercury saturation. Error bars indicate the standard deviation if available. **c** Air- and Ar-derived permeability values related to porosities including error bars (standard deviation) if available and method-specific contours in the background for better data range visibility. **d** Ar permeability distribution across the sampled layers including error bars (standard deviation) if available and **e** is showing the horizontal permeability variation along bed B1 across a normal fault. See Fig. 2B for sample positions in **(d)** and **(e)**

(± 0.3) E–17 m² with a more confined range between 1.2E–17 m² and 2.1E–17 m² was determined for the same samples applying argon gas (Fig. 9A). On average the determined air permeabilities are a factor approximately two times lower than the argon permeabilities with no obvious correlation (Fig. 9A). No correlation between the measured air permeabilities K_{Air} and the maximum hydraulic length l_{max}^h nor the r_{35} (Appendix 1:

Table 4) is noted (Fig. 9B), which also applies to the correlation between the measured argon permeabilities K_{Ar} and the maximum hydraulic length l_{max}^h .

In contrast, a positive correlation between measured argon permeabilities K_{Ar} and the r_{35} is indicated in Fig. 9B. Correlating air permeabilities with porosities derived from various methods shows no distinct relationship between these properties (Fig. 9C). This is also true when comparing the porosity results of all four applied methods with the permeabilities measured with argon gas (Fig. 9C).

The highest K_{Air} values were found in layers B0, B4, and B7, though, similar to the porosity measurements, no vertical (Fig. 9D) or horizontal (Fig. 9E) trends toward the normal fault can be identified from the matrix permeabilities of the sampled beds. Plug permeabilities from the horizontal section (Bed B1, Fig. 9E) consistently show very low values in the range between $7.6E-18$ m² and $14.3E-18$ m² (Appendix 1: Table 4). Furthermore, no permeability trends in N-S, E-W directions, and vertical sampling successions were determined (Appendix 1: Table 4), suggesting that the rocks are behaving relatively isotropically regarding fluid flow. All permeability models applied in this study (Appendix 1: Fig. 11) show at least moderate correlations with measured permeability values. With exception of the CT Model (Appendix 1: Fig. 11E), which is solely based on the BIB-SEM analysis, we only display permeability prediction models based on Φ_{Hg} , Φ_{He} , and Φ_{Ar} for better clarification, as Φ_{Gd} and Φ_{He} , as well as the Φ_{Ar} , Φ_{Hg} , and $\Phi_{BIB-SEM}$ values, show very low variation among each other (Fig. 8A).

Comparing the model-based permeability estimations to air permeability measurements (K_{Air}), decent fits, hence low mean residual square error (MRSE) (Table 1), were achieved for the Katz-Thompson (K-T) Model (Appendix 1: Fig. 11A) and the Winland Model using Φ_{Ar} and Φ_{Hg} (Appendix 1: Fig. 11B). The same applies to the Kozeny-Carman Model (K-C) using the best-fit tortuosity factor of $\tau=1.57$ that was achieved by optimizing the CT Model applying He porosity (Appendix 1: Fig. 11D), and the Bohnsack Model using Φ_{Ar} and Φ_{Hg} (Appendix 1: Fig. 11F). Great fits are achieved for the CT Model (Appendix 1: Fig. 11E) and the Saki Model (Appendix 1: Fig. 11H), both being well within the 2.5 variance factor from the perfect fit. The Winland Model using Φ_{He} (Appendix 1: Fig. 11B), the Dastidar Model (Appendix 1: Fig. 11C), the Bohnsack Model also using Φ_{He} (Appendix 1: Fig. 11F), and the GPPT Model (Appendix 1: Fig. 11G) strongly overestimate the measured permeabilities. In contrast, the Kozeny-Carman Model (K-C) using Φ_{Ar} and Φ_{Hg} (Appendix 1: Fig. 11D) underestimates the air permeability K_{Air} .

In general, similar observations are made when comparing the permeability models to the measured argon permeabilities (K_{Ar}), although with a better correlation. The latter applies except the K-T (Appendix 1: Fig. 11A) and the K-C Models (Appendix 1: Fig. 11D). Particularly well fitting permeability estimations are achieved by applying the Capillary tube (Appendix 1: Fig. 11E) and the Saki Model (Appendix 1: Fig. 11H).

Mechanical properties

We calculated the dynamic elastic parameters (Poisson's number, the dynamic Young's Modulus, and the Bulk Modulus) from sonic velocity measurements using Eqs. (5)–(9), respectively (Table 2). For samples where the shear velocities were not available and hence, the Poisson's number could not be calculated, and the average value of $\nu=0.27$

Table 1 For determining the best permeability estimation model, the mean residual square error (MRSE) in relation to the corresponding air K_{Ar} and argon K_{Ar} permeabilities and standard deviations (σ) for each model and applied porosity method (Archimedes porosity: ϕ_{Ar} ; He pycnometry: ϕ_{He} ; MICP porosity: ϕ_{Hg}) were calculated

Model	ϕ_{Ar}			ϕ_{He}			ϕ_{Hg}			Overall rank											
	K_{Ar}			K_{Ar}			K_{Ar}			K_{Ar}											
	MRSE	σ	Rank	MRSE	σ	Rank	MRSE	σ	Rank	MRSE	σ	Rank	K_{Ar}	K_{Ar}	K_{Ar}						
K-T Model	0.15	0.15	2	0.23	0.26	3	0.13	0.11	1	0.33	0.18	3	0.19	0.18	2	0.20	0.29	3	1	3	
Winland Model	0.36	0.33	4	0.20	0.15	2	0.65	0.44	4	0.42	0.27	4	0.28	0.33	4	0.20	0.16	3	4	3	
Dastidar Model	0.56	0.23	6	0.26	0.14	4	0.89	0.33	6	0.58	0.30	6	0.55	0.36	6	0.35	0.34	4	6	5	
K-C Model	0.44	0.70	5	0.92	1.53	7	0.23	0.25	3	0.32	0.51	2	0.42	0.40	5	0.53	0.73	6	5	6	
Bohnsack Model	0.13	0.21	1	0.29	0.41	5	0.78	0.44	5	0.44	0.28	5	0.21	0.19	3	0.14	0.23	2	3	4	
GPPT Model	0.72	0.32	7	0.30	0.17	6	1.26	0.58	7	0.73	0.20	7	0.69	0.41	7	0.40	0.19	5	7	7	
Saki Model	0.17	0.10	3	0.03	0.02	1	0.20	0.12	2	0.04	0.03	1	0.17	0.11	1	0.03	0.02	1	2	1	
Capillary tube Model	No porosity used																				
	K_{Ar}			K_{Ar}			K_{Ar}			K_{Ar}			K_{Ar}			K_{Ar}			K_{Ar}		
	$\tau = 2.00$			$\tau = 1.57$			$\tau = 2.00$			$\tau = 2.00$			$\tau = 1.57$			$\tau = 1.57$			$\tau = 1.57$		
	MRSE	σ		MRSE	σ		MRSE	σ		MRSE	σ		MRSE	σ		MRSE	σ		MRSE	σ	
	0.06	0.06		0.17	0.14		0.05	0.03		0.05	0.03		0.03	0.00		0.00	0.00		0.00	0.00	

Table 2 Summary of mechanical parameters of Simmelsdorf quarry limestones (Malm β) calculated from P- and S-wave velocities

Bed number	Horizontal	Bed thickness	Distance from fault	Plug	V_p	V_s	v^{dyn}	E^{dyn}	K^{dyn}	G^{dyn}	G^{stat}
[#]	[-]	[cm]	[m]	[-]	[m/s]	[m/s]	[-]	[GPa]	[GPa]	[GPa]	[GPa]
B10		55	-	10_V	5758	3160	0.28	65	51	25	15
B9		22	-	9_V	5808	3190	0.28	67	52	26	15
				9_2V	5957	3328	0.27	74	54	29	17
				C91V	5486	-	0.27*	62	45	24	14
				C91H	5501	-	0.27*	62	45	25	14
				C92H	5506	-	0.27*	63	45	25	14
B8		20	-	8_V	5812	3305	0.26	71	50	28	17
				C8V	5615	-	0.27*	66	47	26	15
				C8H	5767	-	0.27*	69	50	27	16
B7		40	-	7_V	5845	3298	0.27	71	51	28	17
B6.2		15	-	C62V	5583	-	0.27*	64	46	25	15
				C62H1	5604	-	0.27*	65	46	25	15
				C62H2	5725	-	0.27*	67	49	27	16
B6.1		35	-	C61V	5735	-	0.27*	69	49	27	16
				C61H2	5403	-	0.27*	61	44	24	14
B5		40	-	5_V	5730	3275	0.26	69	48	28	16
				C5V	5484	-	0.27*	62	45	24	14
				C5H2	5560	-	0.27*	64	46	25	15
B4		35	-	4_V	5948	3305	0.28	72	54	28	17
				4_2V	5906	3305	0.27	72	53	28	17
B3		32	-	3_V	5849	3338	0.26	73	50	29	17
B2		18	-	2_V	5488	3250	0.23	66	41	27	16
B1	D	45	6.0	1D_V	5991	3385	0.27	76	54	30	18
B1	C	45	4.5	1C_V	5984	3248	0.29	71	57	27	16

Table 2 (continued)

Bed number	Horizontal	Bed thickness	Distance from fault	Plug	V_p	V_s	ν^{dyn}	E^{dyn}	K^{dyn}	G^{dyn}	G^{stat}
[#]	[-]	[cm]	[m]	[-]	[m/s]	[m/s]	[-]	[GPa]	[GPa]	[GPa]	[GPa]
B1	A	45	0.5	1A_V	5733	3195	0.27	67	50	26	15
B1	F	45	- 3.5	1F_V	5717	3263	0.26	69	48	27	16
B1	E	45	- 5.0	1E_V	5866	3453	0.23	77	48	31	18
				1E_2V	6090	3313	0.29	74	59	29	17
B1	G	45	- 6.5	1G_V	6254	3440	0.28	80	61	31	18
B1	H	45	- 8.5	1H_V	5977	3298	0.28	72	55	28	17
B1		45	-	1_V	5985	3370	0.27	75	54	30	17
B0		30	-	0_V	6513	3565	0.29	85	66	33	20
B-1		43	-	-1_V	5865	3218	0.28	69	53	27	16

ν Poisson's number; E^{dyn} Young's Modulus; K^{dyn} Bulk Modulus; $G^{dyn/stat}$ Shear Modulus

See Fig. 2b and c for sample positions

*Poisson's number calculated from samples, where the p-wave (VP) and the s-wave (VS) velocity were available.

derived from all other samples was used. As we achieved very similar velocity values despite the samples were analyzed in two different laboratories, the measurements are considered as reliable. All limestone beds are rated as very homogeneous in terms of their geomechanical properties, with the dynamic E -, K , G_{dyn} , and G_{stat} moduli ranging between 65 and 85 GPa with a mean of 73 ± 5 GPa, 41–66 GPa with a mean of 53 ± 5 GPa, 24–33 GPa with a mean of 27 ± 2 GPa, and 14–20 GPa with a mean of 16 ± 1 GPa, respectively.

The relative porosity and permeability changes at a depth of ~ 2000 m TVD (≈ 25 MPa), corresponding roughly to the burial depth of the Malm reservoir in the SMGB according to Drews et al. (2020), are listed in Appendix 1: Table 5. Based on Eq. (9), a relative porosity change of 0.06% to 0.08% with a mean of $0.07 \pm 0.01\%$ based on the G^{dyn} is to be expected, while calculations using the static shear module G^{stat} suggest a relative porosity change of 0.10% to 0.14%. with a mean of $0.12 \pm 0.01\%$. A larger relative change at same burial depth is predicted for the permeability by applying Eq. (10), using two different values β_{min} ($=28.3$) and β_{max} ($=46.3$) (Bohnsack et al. 2021). The results suggest a relative change Δk_{Min} of 1.65% to 2.27% with a mean of $2.01 \pm 0.15\%$ and Δk_{Max} of 2.69% to 3.69% with a mean of $3.27 \pm 0.24\%$ using G^{dyn} . In contrast, a permeability change of 2.77% to 3.88% (mean $3.41 \pm 0.27\%$) for Δk_{Min} and of 4.50% to 6.26% (mean $5.52 \pm 0.43\%$) for Δk_{Max} based on the static shear module is to be expected.

Discussion

Pore throat size and pore connectivity

The BIB-SEM porosity, as well as the LMI-BIB-SEM observations regarding the filling of almost the entire visible open pores at high injection pressure (Fig. 6), indicate that a significant part, if not the entire BIB-SEM porosity, is connected. This is in good agreement with the similarity of the average BIB-SEM porosity and the average MICP porosity values (Fig. 8C and D). Moreover, comparing the mean pore size from BIB-SEM (~ 500 nm, Fig. 7) with mean pore throat sizes from MICP (~ 11 nm and ~ 33 nm, Fig. 3) results in pore body to pore throat (aspect) ratios of about 25:1. According to Zhao et al. (2018), who also apply MICP, such ratios for tight carbonates are typically in the range of c. 40:1 to 480:1, with small ratios, indicating increased conductivity to fluid flow compared to large ratios. From our ratio, we propose higher permeabilities for tight carbonates when compared to matrix permeability values of $2.3\text{E}-19$ to $2.0\text{E}-20$ m^2 , determined for similar rock types by Hu et al. (2020). However, the ratio only allows for a qualitative statement. For example, Cai et al. (2019) have shown that tortuosity and connectivity, among others, play a significant role in controlling hydraulic flow in porous media. Using the ratio as the sole factor for permeability estimation is therefore not advisable. Overall, the negligible variations in pore volumes, pore throat sizes, and pore size distribution with varying distances to the fault (Figs. 3B and 8C) imply that faulting and fracturing are essentially post-diagenetic.

Microstructure and pore geometry

Submicron interparticle and intercrystalline pores of sub-angular shape are the most abundant types of pores within the matrix of Malm β limestones. Also, elongated interparticle pores are present, as well as moldic pores, which resulted from the dissolution

of the still recognizable fossil remnants but are relatively rare though can be relatively large in size (Fig. 6). The elongated open void spaces are associated with stylolites that are interpreted to have re-opened due to stress release and/or desiccation. The pores at the stylolite interfaces alternate with the accumulation of insoluble, dense minerals mainly at their peaks (Fig. 5E and F), coinciding with the observations of, e.g., Heap et al. (2014) and Toussaint et al. (2018). These authors assign a complex internal structure of varying thickness to these stylolites, which are interpreted to be a product of the horizontal linkage and vertical coalescence of multiple pressure solution seams (Nenna and Aydin 2011; Toussaint et al. 2018). Hence, our findings confirm the microporous nature of stylolites, which can significantly contribute to the total porosity of low-porous carbonates, at least under unconfined stress conditions. However, due to their elongated shape, it is reasonable to assume that these structures will successively be closed with increasing effective stress (Si et al. 2018). This applies to cases where the principal stress is directed perpendicular to the longitudinal axis of the stylolite and hence to the elongated pores, which are typically arranged parallel to the stylolites. Such an assumption is emphasized by the continued mercury intrusion at the device's maximum pressure (Fig. 3), reflecting either the closure of pores or microfractures or suggesting that some of the open pore space still acts as flow paths for the intruding fluid.

Porosity

A comparison between the various porosity measurement methods shows general conformance among the results with values between 2 and 5% (Fig. 8A), and also with published data for mud-supported limestones (mud- to wackestones) of the same Malm β stratigraphy from outcrops on the Southern and Northern Franconian Alb (Homuth et al. 2014, 2015; Mraz et al. 2018) and the subsurface of the SGMB (Beichel et al. 2014; Böhm et al. 2010; Bohnsack et al. 2020). Neither across the vertical sampled limestone section nor along an individual layer (B1) in a horizontal section, significant changes in the mean matrix porosity were visible (Fig. 8C). This in turn suggests that the petrophysical properties can be considered as rather constant in the investigated section. We think that a missing matrix porosity gradient toward faults is mostly related to both the prevailing stress conditions and the rock's high strength, which promoted dilatant fractures/faults. This, in turn, resulted in localized fluid flow through these structures and prevented the alteration of the tight matrix. Particularly well matching are Φ_{Gd} and Φ_{He} values with only minor method-related deviations (Fig. 8A and B). In contrast, Φ_{Ar} , Φ_{Hg} , and $\Phi_{BIB-SEM}$ values for the same samples are (Fig. 8A) uniformly lower.

Deviations in porosity values are likely related to the capability of the measurement device to register total porosity (e.g., including isolated pores) or only effective porosity (selectively recording connected pores). Also, injection/saturation methods apply different fluids with pore-scale fluid occupancy and connectivity being controlled by surface roughness, intrinsic (wetting) contact angle of the fluid, the wetting state, and the spatial distribution of wettability (Armstrong et al. 2021). Physical limitations in the injection or a negative pressure may prevent the detection of pores below a diameter of 3 nm (MICP) and slightly smaller pores (Archimedes method) (Clarkson et al. 2013; Giesche 2006; Kiula et al. 2014; Okolo et al. 2015; Webb 2001). Full saturation even at the devices' technical limits cannot be ensured with absolute certainty, as air might still be trapped

at isolated and dead-end pores. In contrast, the bulk gamma density and the BIB-SEM method are not affected by this problem, with the latter method being only limited by its maximum resolution (≥ 10 nm). However, this should not play a significant role, as it is clear from the pore size distributions of our samples that the majority of pore space is in the 0.1–1 μm range (Figs. 3 and 7B).

Keeping the method drawbacks in mind, our observations indicate a low ratio of isolated pores within the matrix, inferred from only slight differences between Φ_{Gd} and Φ_{He} values (Fig. 8A) and the rare presence of unconnected pores in the LMI-BIB-SEM visualization. The He pycnometry provides the most reliable values for the effective porosity, while the bulk gamma density method detects additional isolated pore space. Regarding the determination of effective porosity for geothermal applications, the Archimedes method provides the most practical method.

Permeability and permeability models

Although fluid flow in tight carbonates is primarily controlled by dissolution and structural features such as faults, fractures, and fracture corridors (Al-Obaid et al. 2005; Dimmen et al. 2017; Litsey et al. 1986; O'Neill 1988; Zeybek and Kuchuk 2002), matrix porosity can be a significant reservoir for fluid recharge. Therefore, different permeability measurement methods and permeability prediction models will be discussed regarding their reliability and limitations.

Permeability

A large spread in air permeabilities ($1.9\text{E}-18$ m² to $10.8\text{E}-18$ m²) most likely results from device-related issues, such as relatively low confining and injection pressures and the missing Klinkenberg correction of the air permeabilities. This also leads to a deviation from the argon permeabilities ($1.2\text{E}-17$ m² to $2.1\text{E}-17$ m², Fig. 9A). Surprisingly, a missing Klinkenberg correction should rather result in increased than in lower permeabilities, as it is the case here. No laminar flow may have been established during the air permeability measurements, despite measurements were only initiated after fluid flow did no longer show large variations. A similar problem is reported by Bohnsack et al. (2020) for mud-supported limestone (mud- to wackestone) samples which are comparable to ours. As this problem seems to be common for low- to ultralow-permeable reservoir rocks, unsteady-state permeability measurement methods (e.g., pulse decay, oscillating pressure, GRI method) on these rock types are frequently preferred over the steady-state methods (Sander et al. 2017). Methodological studies by Boulin et al. (2012), Chenevert and Sharma (1993), and Bertinello and Honarpour (2013), however, on low- to ultralow-permeable (unconventional gas) reservoir rocks have concluded that the steady-state method is still more reliable than for instance the pulse decay method. Thus, the best practical solution for permeability measurements on low-permeable rocks is still matter of debate (Sander et al. 2017). We consider our data set as reliable as permeability values of a similar range were determined for the same sample set in different laboratories and by different methods.

The missing correlation between porosity and air/argon permeability values (Fig. 9C) suggests that fluid flow through the matrix primarily depends on pore connectivity and pore throat size distribution rather than on the effective porosity. This is in accordance

with results of Smodej et al. (2020), showing that the permeability is mostly controlled by the smallest throats. The slightly positive correlation between the argon permeabilities and the r_{35} also points to the pore throat size distribution, particularly the r_{35} , as the matrix permeability-controlling factor, thereby agreeing with the findings of Saki et al. (2020). However, a statement regarding the importance of the pore throat size distribution as a whole or particular pore throat diameters (e.g., l_{\max}^h or the r_{50}) for the matrix permeability cannot be made due to a strongly confined range of permeabilities and pore throat diameters (Fig. 9B).

No influence on the matrix permeability was observed in case of the presence of stylolites, regardless of their orientation with respect to the measurement direction. This is in contrast to the findings of Heap et al. (2014) or Hu et al. (2020), who related increased permeabilities to the presence of stylolites. Other authors (e.g., Mehrabi et al. 2016; Rashid et al. 2017; Vandeginste and John 2013) consider stylolites primarily as barriers to fluid flow, depending on their roughness profile (Koehn et al. 2016). This highlights the ambivalent nature of these structural features, as already described by various authors (e.g., Bruna et al. 2019; Burgess and Peter 1985; Korneva et al. 2014; Toussaint et al. 2018). Nevertheless, it is most likely that the stylolite fillings have a lower permeability as the carbonate matrix, as the microstructure of the stylolite filling (Fig. 5D) corresponds to that of porous clays or claystones with permeabilities in the same order of magnitude.

Overall, faulting and fracturing had no noticeably effect on the permeability of the surrounding protolith, at least at the scale of this investigation. We relate this to the post-diagenetic timing of faulting and the limestones overall low permeability, which inhibits intensive fluid–rock interactions, such as karstification or leaching due to the negligible exchange of percolating fluids. Ziauddin and Bize (2007) experimental results support this, as they found limestones of the Khuff formation with similar petrophysical properties compared to the investigated samples to be insensitive to matrix acidizing due to their too low permeabilities.

Permeability models

As illustrated in Appendix 1: Fig 11, most applied permeability prediction models correlate relatively well with measured permeabilities (K_{Ar} and K_{Air}). However, except for the CT and the Saki Models, the variation of the predicted permeabilities is at least one order of magnitude. As permeabilities measured with argon gas are about twice as high as permeabilities measured with air (Fig. 8A), the difference between these methods is low with a slight trend of K_{Air} toward lower permeability values. Still, some models, such as the CT Model and the Saki Model, show a better correlation to measured permeabilities than others, particularly when applying argon for permeability measurements.

The very good fit of the CT Model (particularly with $\tau = 1.57$) with the measured permeabilities (Appendix 1: Fig 11) is primarily related to the involved parameters, namely, the tortuosity τ , the hydraulic radius r_p , and the porosity of each segmented pore Φ_p , all derived from BIB-SEM analysis. In contrast to other permeability prediction models (except the K–C Model), the CT Model does neither integrate additional empirically determined constants nor porosity values from any of the applied porosity measurement methods. It is most likely for this reason that permeabilities calculated by the CT Model correlate well with the measured permeabilities (Appendix 1: Table 5). The fact that the K–C Model performs worse in terms of the match of

predicted with measured permeabilities, despite avoiding the integration of empirical parameters, is most likely related to two facts: firstly, the CT Model has been continuously refined along with improving technical possibilities over the last decades. And secondly, the specific surface area S_o was measured with the MICP, which might lead to an underestimation at high injection and confining pressures due to the closure of microfractures and stylolites, all resulting in inaccurate permeability predictions. We, therefore, think that the three parameters (τ , r_i , and Φ_i) are quite important regarding the assessment of fluid flow within the matrix.

A very good correlation between predicted and measured permeabilities is also achieved by the Saki Model (Appendix 1: Fig 11H). The fact that this model (Saki et al. 2020) applies the smallest pore/throat radius r_{35} among other parameters points to the high importance of the r_{35} , as a decisive factor in controlling the matrix permeability. Even though the Winland Model (Appendix 1: Fig 11B) also applies the r_{35} parameter this results in a worse prediction/measurement match. This suggests that either the calibration samples used by Saki et al. (2020) are more similar to the samples investigated in our study than the ones used by Winland (Comisky et al. 2007; Gunter et al. 2014; Rashid et al. 2015), or rather that this parameter's impact on the Saki equation (Eq. 15) is larger than in the Winland equation (Eq. 9). Nevertheless, the first reason for a worse fit of the model is, in our opinion, the main controlling factor for the deviation of most model-based predictions (K–T, Dastidar, Bohnsack, and the GPPT Models) from measured permeabilities as all of them apply parameters that were empirically determined on the specific data set. Using different petrophysical rock characterization methods for the model calibration might lead to further deviations (e.g., Bohnsack Model). Whether the Saki Model represents the best permeability estimation model for tight carbonates, in general, is therefore questionable and has to be investigated in further studies on other tight carbonates, as this model also incorporates various constants calibrated on their specific data set.

Other models, such as the K–T and the Dastidar Models, which also use pore throat radii at a specific saturation (K–T Model) or capillary pressure (Dastidar Model) correlate significantly worse with measured permeabilities compared to the CT and the Saki Models, suggesting once more that the r_{35} parameter is an important matrix permeability-controlling factor, at least in the case of the samples investigated in this study. Although other studies propose that the permeability in tight limestones is primarily controlled by the pore throat radii (Cai et al. 2019; Zhao et al. 2018) or the smallest pore body sizes (Smodej et al. 2020) rather than by the entire effective porosity range, this does not contradict our results. Instead, our results are rather complementary to these findings and specify that one particular pore throat radius, namely, the r_{35} , has a particularly strong control on fluid flow in the matrix.

Implications for matrix permeability-controlling factors Relationships between the various petrophysical parameters lead to the following conclusions. As indicated by the overestimation of predicted permeabilities that use the more accurate He porosity values, microporosity does not have a significant impact on the rock's matrix permeability. As the He porosity, which is higher compared to the Ar, MICP, and BIB-SEM porosities due to the registration of microporosity, is integrated in permeability calculations as a multiplication factor (K–T model), as an exponential factor (Winland,

Dastidar, K-C, and Bohnsack Models), or as logarithmic factor (Saki and GPPT Models), the predicted permeabilities are also elevated. Resulting permeability predictions deviating from measured permeabilities, therefore, implies a negligible effect of microporosity, but a higher importance of the pore throat size distribution and the pore network connectivity, conforming to the conclusions by Lala and El-Sayed (2017) and Philipp et al. (2017). In particular, the pore throat radius at a mercury saturation of 35% (r_{35}) seems to be the parameter controlling most to the fluid flow in the pore network, as both best-performing models (Winland and Saki) integrate this measure. Also, a correlation between argon permeabilities and the r_{35} could be found, though without a clear trend due to the confined value range (Fig. 9B).

We can further conclude that most permeability prediction models deviate from the measured permeabilities due to the involvement of empirically determined variables that were calibrated on rock sample sets of slightly different lithologies, derived from locations that experienced a different diagenetic history compared to our samples. Also misleading appears the application of effective porosity as the sole physical input parameter, as this is not the main permeability-controlling factor according to Cai et al. (2019) and Zhao et al. (2018). Fluid flow in pore networks also strongly depends on the wettability of the permeating fluid/gas, on the spatial distribution of the wettability, which is related to the type of minerals present in the sample, as well as on the surface roughness (Armstrong et al. 2021). Both the spatial wettability distribution and the surface pore roughness are difficult to quantify and were not available in this study. This fact and the complex interrelation of these factors impede reliable permeability predictions, as most permeability prediction models applied in this study—except for the Capillary Tube and the Bohnsack Model—try to approximate the permeability based on MICP-derived pore throat diameter distributions, which in turn depend on the above mentioned permeability-controlling factors proposed by Armstrong et al. (2021). As these factors also concern the permeability measurement itself, the permeability prediction derived from measurements that use different permeating fluids will always be prone to inaccuracies unless detailed information on the wettability distribution, the fluid's wettability, and the surface roughness of the sample is considered.

Model rating To quantify the performance of the various models for permeability estimation, the Mean Residual Square Error (MRSE) was calculated for each model and each porosity-determining method (Appendix 1: Table 5) as illustrated in Fig. 10. We will only compare our rankings of the models' performances in the context of argon permeabilities to the rankings of other authors from here on, as the argon permeabilities proved a greater reliability compared to air permeabilities.

Based on the MRSE, a ranking for each method and an overall comparative ranking is determined (Table 1). The CT Model could not be taken into account as it does not use a bulk porosity method. Relating the permeability predictions to the measured air permeabilities K_{Air} (Fig. 10A) provides satisfying results for the K-T (overall rank 1), the Saki (overall rank 2), and the Bohnsack Models (overall rank 3). A slightly different rating results from models using Φ_{Ar} and Φ_{Hg} , where both the K-T (rank 1) and

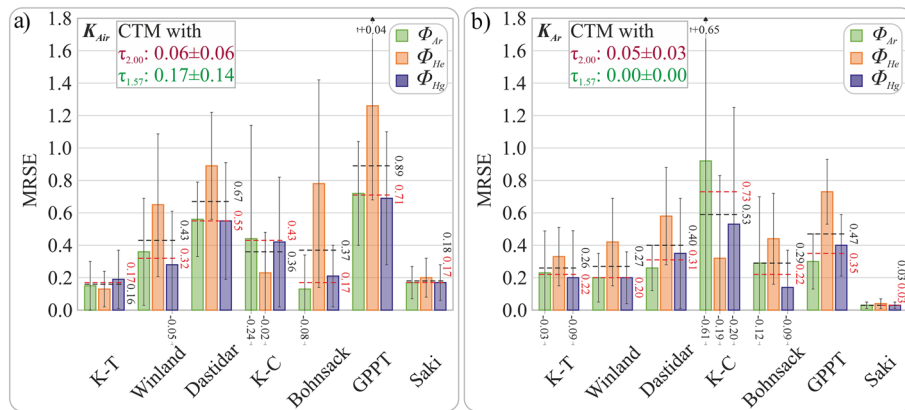


Fig. 10 Grouped bar charts of the mean residual square error (MRSE) including error bars (standard deviation) in relation to **a** the corresponding air permeabilities K_{Air} and **b** argon permeabilities K_{Ar} for each model and the application of different methods for porosity determination (Φ_{Ar} , Φ_{He} , Φ_{Hg}). The corresponding standard deviations are indicated by vertical black bars. If standard deviations are out of diagram range, the missing values are indicated. The mean MRSE of each model applying across all porosities and across only Φ_{Ar} and Φ_{Hg} is highlighted as black and red lines with corresponding values, respectively. The corresponding values are listed in Appendix 1: Table 5

the Bohnsack Models (rank 1) perform equally well, and the Saki Model (rank 3) a little worse (Fig. 10b).

While the comparison to argon permeabilities K_{Ar} (Fig. 10B) shows best correlations with the Saki Model (overall rank 1), both the Winland (overall rank 2) and the K–T Models (overall rank 3) achieve slightly lower rankings. Again, a slightly different ranking order results when only models applying Φ_{Ar} and Φ_{Hg} are considered. The Saki Model (rank 1) performs best and the Winland (rank 2) as well as the Bohnsack and the K–T Models (both rank 3) show good correlations with the measured argon permeability. The CT Model is always among the top four prediction models. Hence, we recommend using either the Saki or the CT Model for estimating permeabilities of similar sample lithologies.

The comparison of our permeability estimation model ranking to rankings of Comisky et al. (2007) and Rashid et al. (2015) shows some similarities, although the spectrum of their models differs from ours. Comisky et al. (2007) for instance found a good correlation between measured and modeled permeabilities based on the K–T method (their rank 2) and the Winland method (their rank 5), whereas these models achieved ranks 3 and 2 in our comparison.

Those models that were applied by both our study and that of Rashid et al. (2015) are the Winland (their rank 4), the K–T (their rank 9), and the Dastidar Models (their rank 12). Although a comparison of their ranking results to our ranking is hardly representative, their relative ranking order differs from ours, as the K-T Model performed very well in the case of our data set. Nevertheless, even the best-performing permeability estimation model (generic model) in the ranking of Rashid et al. (2015) still has a mean residual square error of 0.402 and therefore shows a poorer correlation to measured permeabilities than the CT and the Saki Models.

Implications for a “best practice” in the petrophysical analyses of tight carbonates We conclude from our data set that porosity data for permeability models are best acquired by mercury intrusion porosimetry, or even better, LMI-BIB-SEM, as this method provides not only reliable information on the porosity (the connected pore volume relative to the bulk rock volume) but, compared to other methods (e.g., NMR, SEM, X-ray CT), also on a larger range of pore throat sizes (Wu et al. 2019). Pore throat sizes (particularly the r_{35}) exercise primary control over matrix permeability and are therefore an indispensable prerequisite for a reliable permeability estimation. Although a larger pore size range is accessed and measured through Helium pycnometry, Mercury intrusion porosimetry offers a wider range of applications as also the permeability can be estimated quite accurately, even from small sample volumes, such as drill cuttings. Hence, even when the availability of sample material is limited, the rock's matrix permeability can be estimated, which is particularly useful for subsequent modeling purposes. However, special care should be taken regarding the presence of microfractures induced by sample handling. Ideally one should investigate the sample after injection, for example by employing LMI-BIB-SEM, as this method is well suited for the detection of microfractures and injection-related artifacts.

Mechanical properties and the relation of petrophysical properties to buried samples

All samples that were investigated in terms of their rigidity revealed similar values in the range of 65 to 86 GPa (Young's Modulus, Table 1). Geomechanical measurements on rocks from the same stratigraphic units (Malm α and β) and of comparable lithology (mud- to wackestone), but buried 240–5200 m TVD in the SGMB were carried out by Potten (2020) showing values of a similar range (70 to 74 GPa), confirming the comparability of outcrop analog and buried tight carbonates, at least in this particular case. The rock's stiffness depends mostly on the pore type, pore geometry, and the total porosity (Eberli et al. 2003; Li et al. 2018; Weger et al. 2004). These parameters, together with pre-existing zones of weakness, such as stylolites (e.g., Agosta et al. 2015; Antonellini et al. 2008, 2014; Graham et al. 2003; Micarelli et al. 2005; Tondi 2007) and the in situ effective stress conditions control the deformation mode and the resulting fault zone structure and consequently its hydraulic capacity to conduct fluids (e.g., Antonellini et al. 2008; Michie 2015; Sagi et al. 2016). The majority of the samples' pores were found to be of the submicron interparticle, intercrystalline, and occasionally also of the moldic small mesopore type, and of (tri-)angular pore geometry. All determined properties in combination with the low total porosity explain the very high mechanical strength of the investigated rocks (Eberli et al. 2003; Potten 2020).

Relating the mechanically very competent limestones from Frankenalb outcrop analogs to reservoir depths, which in case of the SGMB would be > 2000 m TVD toward the south of Munich (Mraz 2019), a relative volume change of only 0.06% to 0.08% or 0.10% to 0.14% is calculated (see Appendix 1: Table 5), depending on whether G^{dyn} or G^{stat} (Eqs. 17 and 19) are used for calculations. In contrast, Bohnsack et al. (2021) determined a relative porosity change of ~ 2% when buried ~ 2 km TVD, hence one order of magnitude larger. This large discrepancy is most likely related to the fact

that porosities and geomechanical parameters of their investigated reservoir rocks (Grainstones from the Malm ζ 4–5) differ significantly from our samples (higher porosity, but lower rock stiffness/strength), which strongly increases their sensibility to effective stress changes. This highlights the importance of pore geometry and pore connectivity in relation to geomechanical properties and the stress sensitivity, a dependency has been thoroughly investigated by various authors (e.g., Zoback and Byerlee 1975; Pei et al. 2014; Xu et al. 2018a, b).

Comparing our relative permeability changes Δk_{Min} (1.65% to 2.27%) and Δk_{Max} (2.69% to 3.69%) calculated with G^{dyn} or Δk_{Min} (2.77% to 3.88%) and Δk_{Max} (4.50% to 6.26%) calculated with G^{stat} to those of Bohnsack et al. (2021) (33.0% to 56.7%) again shows that for our rocks, the permeability change is about one order of magnitude smaller than the values determined by Bohnsack et al. (2021) or other authors investigating similar rock types (e.g., Bakhtiari et al. 2011; David et al. 1994; Moosavi et al. 2014; Hu et al. 2020). As the stress sensitivity of permeability is a function of porosity (Cheng 2016) and mainly dependent on the aspect ratio, type and size of pores, and pore throats (Rashid et al. 2017) as well as the presence of fracture-like pores or cracks (Bohnsack et al. 2021), permeability change with increasing effective stress is typically higher than porosity change. The permeability reduction is thereby caused by the size reduction of voids, pore closure, pore throat collapse, and/or clogging of pores (Selvadurai and Głowacki 2008). Low-porous carbonate rocks with nano-intercrystalline pore types and high aspect ratio pores should therefore be much more sensible to effective stress-induced permeability reduction (c.f., Rashid et al. 2017).

As the rocks investigated in this study are already strongly lithified and consequently have very high elastic moduli, low porosities, and low pore throat diameters in relation to the samples investigated by Bohnsack et al. (2021), they are much more resistant to effective stress-induced deformation. Together with the comparatively low aspect ratios for these types of rocks found by Zhao et al. (2018), the significantly lower sensitivity to effective stress associated with low porosity/permeability changes with increasing effective stress can be explained. It has to be considered that the static Shear Modulus (G^{stat}) was calculated based on an empirical relationship identified by Bastos et al. (1998) and these values are therefore prone to inaccuracies due to lithological and petrophysical differences. Studies by Homuth and Sass (2014) as well as Pei et al. (2014) on rocks lithologically and stratigraphically similar to those of our study showed that other than the effective stress, rather the prevailing temperature at reservoir level (≥ 60 °C) appears to control the permeability reduction due to thermal expansion. As the rocks investigated in this study are all low porous and primarily composed of rock matrix, thermal expansion with increasing depth and temperature might have a much larger impact on the petrophysical properties of these rocks at depth than the effective stress.

Consequently, stress conditions at reservoir level should hardly influence the petrophysical properties of the limestone matrix. Rock matrix petrophysical properties measured at surface conditions should therefore be well relatable to properties at reservoir level. Lower porosities measured by Bohnsack et al. (2021) at 25 MPa confining stress ($\sim 2.0\%$) compared to the porosities measured at atmospheric conditions ($\sim 3.3\%$) by Homuth et al. (2014) and by us (2.9–3.2%) of the same stratigraphic unit likely relate to changes in lithology (mud-supported limestones), different degrees of dolomitization related to regional heterogeneities of the depositional system, and variation in diagenetic alteration processes (Bohnsack et al. 2020). As the differences in porosities are very low,

these factors are thought to play a minor role in their influence on the petrophysical properties, at least in the case of Malm β carbonates. Also, as according to our findings, the pore throat distribution is controlling the matrix permeability rather than the effective porosity, these small differences in porosity should be negligible and are considered as intrinsic sample heterogeneities. Thus, we are confident that our results reflect a good estimation of in situ petrophysical properties due to the rocks' high stiffness.

Conclusion

In this study, petrophysical properties and microstructures of tight carbonates were investigated with various methods, aiming for characterizing the matrix properties of the Upper Jurassic (Malm β) limestones in Northern Bavaria for modeling purposes and deriving correlations between the different measurements using various models. Furthermore, their interdependence of the protolith's porosity with stylolitization and normal fault distance were examined. The overall average porosity measured by MICP, He, GD, BIB-SEM, and Archimedes methods is $3.1 \pm 1.0\%$ and the overall average gas permeability is $1.4E-17 \text{ m}^2$, defining them as tight carbonates. Nevertheless, it has to be considered that the effective porosity, e.g., for geothermal applications is expected to be much lower than the measured values as the percolating fluids are thermal waters or brines, for which the microporosity can be neglected in terms of its importance for subsurface fluid transport within the matrix. No significant impact of stylolites on the permeability and porosity under confined conditions was observed. Furthermore, no improved petrophysical properties in a preferred direction were recorded, indicating a homogeneous, isotropic behavior of the rock. Normal faulting had no observable impact on the matrix's poro-perm properties at the meter scale. We, therefore, assume post-diagenetic fracturing and faulting, as otherwise faulting-related processes would have most likely altered the petrophysical properties of the rock matrix. Few leached pores were observed, but with negligible effect on porosity and permeability. The majority of the porosity is in the submicron range. Two models, the CT Model and the Saki Model for estimating permeability from porosity and pore size distribution data, obtained from either the MICP or the BIB-SEM method, gave best results compared to measured permeabilities (air and argon) for the examined rock types. The CT Model applies a tortuosity factor of 1.57 fitted from BIB-SEM analyses, while the Saki Model integrates the pore throat size at 35% mercury saturation. We found that the pore throat diameter is a main factor controlling fluid flow in the rock matrix rather than the effective porosity or microporosity. The application of other models developed by Katz-Thompson (K-T), Winland, and Bohnsack et al. using Ar and MICP porosities also results in reasonable permeability estimations. Due to the relative high rock stiffness of $\sim 73 \text{ GPa}$ for the dynamic Young's Modulus, $\sim 53 \text{ GPa}$ for the dynamic Bulk Modulus, 27 GPa for the dynamic and 16 GPa for the calculated static Shear Modulus our findings can be reliably transferred to reservoir conditions (even at up to 2000 m depth), as the volumetric change of porosity (maximum 0.12%) and of permeability (maximum 5.52%) due to effective stress at this depth are negligibly small.*Poisson's number calculated from samples, where the p-wave (V_p) and the s-wave (V_s) velocity were available

Appendix 1

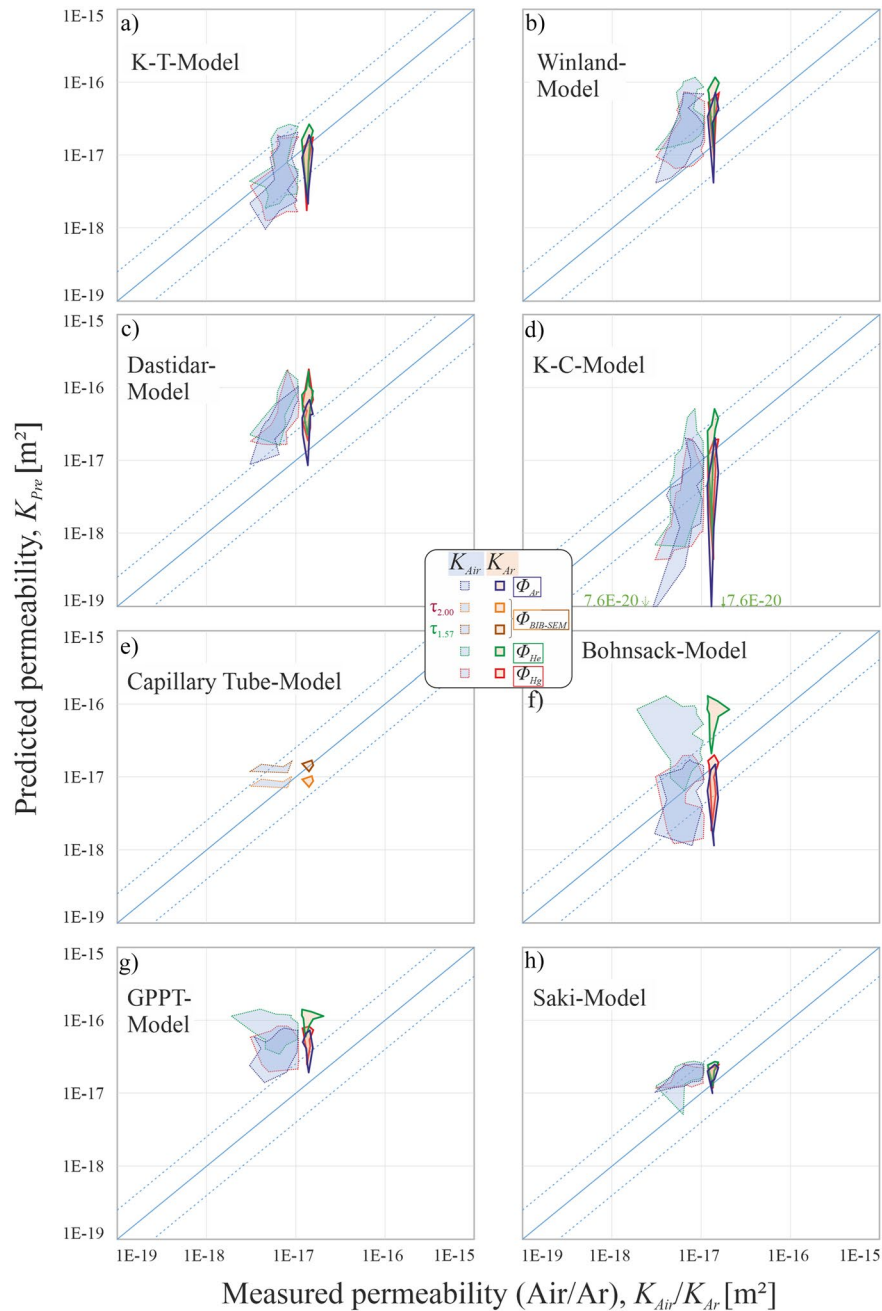


Fig. 11 Correlation between measured permeabilities (by using air K_{Air} or argon K_{Ar} as permeating fluid) and predicted permeabilities (K_{pre}). Tested models are as follows: **a** the Katz-Thompson Model (K-T Model), **b** the Winland Model, **c** the Dastidar Model, **d** the Kozeny-Carman Model (K-C Model), **e** the capillary tube model, **f** the Bohnsack Model (Lms) for mud-supported limestones, **g** the Global Porosity-Permeability Transform (GPPT Model), and **h** the Saki Model. The dashed lines indicate a variation factor with a value of 2.5 from a perfect fit. Except for the capillary tube model **e** permeability measurements and permeability calculations were done on the same samples applying porosities derived from different measurement methods (ϕ_{Hgr} , ϕ_{Her} , ϕ_{Air} and $\phi_{BIB-SEM}$)

Table 3 Summary of measured porosity, bulk and matrix density values of all Simmelsdorf quarry Malm β samples (n = 40). See Fig. 2 for sample positions

Bed	Horizontal	Bed thickness	Distance from fault	Plug label*	Φ _{Ar}	Φ _{Gr}	Φ _{He}	Φ _{Hg}	BIB-SEM porosity @20kx	Bulk density		Matrix density	
										Ar	GR	He	Ar
[#]	[-]	[cm]	[m]	[-]	[%]	[%]	[%]	[%]	[%]	[g/cm ³]	[g/cm ³]	[g/cm ³]	[g/cm ³]
B10		55	-	10_NS	3.54		4.57 ± 0.03	4.11		2.569	2.550	2.681 ± 0.001	2.663
B9		22	-	C91H	2.86	5.58 ± 0.05	5.77 ± 0.07			2.589	2.559	2.728 ± 0.090	2.665
				C91V	3.09	5.15 ± 0.16	5.11 ± 0.16	3.47		2.573	2.569	2.716 ± 0.170	2.655
				C92H	3.06	5.31 ± 0.04	5.36 ± 0.01	4.18		2.580	2.566	2.723 ± 0.010	2.662
				9_NS	3.79		5.45 ± 0.03	2.03		2.572	2.607	2.689 ± 0.001	2.674
				9_2_NS	3.11		3.17 ± 0.03			2.600		2.682 ± 0.002	2.683
B8		20	-	C8H	1.98	3.68 ± 0.40	4.05 ± 0.08	3.54		2.615	2.610	2.715 ± 0.070	2.668
				C8V	3.10	4.50 ± 0.20	3.94 ± 0.06		2.46	2.599	2.588	2.713 ± 0.050	2.682
				8_NS	2.79		3.54 ± 0.01	2.56		2.587	2.559	2.672 ± 0.004	2.661
				8_EW	2.70		2.86 ± 0.01			2.569		2.646 ± 0.007	2.640
				8_V	3.38		3.87 ± 0.02			2.577		2.677 ± 0.001	2.667
B7		40	-	7_NS	3.32		3.95 ± 0.02	2.35		2.589	2.551	2.686 ± 0.002	2.678
B6.2		15	-	C62V	3.17	5.55 ± 0.26	5.71 ± 0.07	3.97		2.584	2.567	2.732 ± 0.080	2.669
				C62H2	1.12	5.11 ± 0.10	5.32 ± 0.21		3.52	2.605	2.572	2.732 ± 0.240	2.635
				C62H1	3.33	5.89 ± 0.15	6.05 ± 0.04			2.588	2.551	2.727 ± 0.080	2.677
B6.1		35	-	C61V	1.66	3.66 ± 0.19	3.95 ± 0.03			2.610	2.611	2.712 ± 0.030	2.654
				C61H2	1.75	4.11 ± 0.19	4.23 ± 0.15	4.39	2.75	2.613	2.599	2.711 ± 0.140	2.659
				6_NS	3.92		5.48 ± 0.02	3.35		2.579		2.698 ± 0.003	2.684
B5		40	-	C5H2	2.86	5.32 ± 0.08	5.00 ± 0.03	4.08		2.586	2.566	2.721 ± 0.030	2.662
				C5V	3.48	5.67 ± 0.06	5.45 ± 0.06		2.12	2.576	2.557	2.721 ± 0.070	2.669
				5_NS	4.01		4.44 ± 0.01	2.98		2.576		2.695 ± 0.002	2.684
				5_V	4.18		4.80 ± 0.02			2.573		2.696 ± 0.001	2.685

Table 3 (continued)

Bed	Horizontal	Bed thickness [cm]	Distance from fault [m]	Plug label*	Φ _{Ar} [%]	Φ _{Gr} [%]	Φ _{He} [%]	Φ _{Hg} [%]	BIB-SEM porosity @20kx [%]	Bulk density [g/cm ³]			Matrix density [g/cm ³]		
										Ar	GR	MICP	He	Ar	
B4		35	-	4_NS	395		4.62±0.02	3.42		2.577	2.588	2.697±0.001	2.683		
B3		32	-	4_2_NS	359		5.97±0.05			2.587		2.701±0.002	2.683		
				3_EW	353		3.91±0.02	2.98		2.505	2.701±0.002	2.706			
B2		18	-	2_NS	381		5.38±0.01	4.31		2.548	2.533	2.685±0.002	2.649		
B1	D	45	6.0	1D_NS	278		3.74±0.01	2.08		2.604	2.669	2.689±0.003	2.678		
B1	C	45	4.5	1C_NS	272		2.98±0.02	1.82		2.607	2.647	2.684±0.004	2.680		
B1	B2	45	3.5	1B_2_NS	323		4.47±0.03			2.568		2.675±0.004	2.654		
B1	B1	45	2.0	1B_1_NS	315		3.33±0.02	2.14		2.606	2.638	2.683±0.003	2.691		
B1	A	45	0.5	1A_NS	202		2.48±0.01	2.68		2.579	2.652	2.625±0.006	2.632		
B1	F	45	-3.5	1F_NS	229		3.56±0.01	3.39		2.589	2.630	2.664±0.001	2.650		
B1	E	45	-5.0	1E_NS	310		3.76±0.01	1.76		2.601	2.628	2.690±0.002	2.684		
B1	G	45	-6.5	1G_NS	212		2.80±0.00	1.94		2.741	2.651	2.671±0.003	2.800		
B1	H	45	-8.5	1H_NS	381		4.44±0.02	2.33		2.576	2.676	2.691±0.002	2.678		
B1		45	-	1_NS	278		3.45±0.01	1.97		2.609	2.590	2.685±0.002	2.683		
				1_EW	288		3.15±0.02			2.658		2.687±0.002	2.736		
				1_V	326		4.07±0.01			2.604		2.687±0.001	2.692		
B0		30	-	0_V	261		3.33±0.01	1.89		2.597	2.559	2.693±0.002	2.672		
B-1		43	-	-1_NS	410		5.21±0.02			2.577		2.695±0.002	2.687		
Number of measurements					40	12	40	24	5	40	24	40	40		

* The plugs with bold labels contain clear stylolites at macroscale. The plug label extensions NS, EW, or V refer to the orientation of the plugs

Table 4 Summary of various pore throat diameter parameters that are subsequently used for certain permeability estimation models, as well as the measured permeabilities

Bed [#]	Horizontal [-]	Plug label* [-]	r_{Main} [nm]	l_{max}^h [nm]	r_{35} [nm]	Ar Permeability, K_{Ar} [m ²]	Air Permeability, K_{Air} [m ²]
B10		10_NS	33.55	20.58	14.15		6.39 E-18 ± 7.40E-19
B9		C91H				1.51E-17	
		C91V				1.24E-17	9.02E-18 ± 1.19E-18
		C92H	19.91	14.13	10.56	1.20E-17	9.09E-18 ± 9.67E-19
		9_NS	12.18	10.68	7.72	1.32E-17	7.82E-18 ± 7.81E-19
B8		9_2_NS					
		C8H	4.93	3.72	4.45	1.37E-17	3.11E-18 ± 2.15E-19
		C8V				1.27E-17	
		8_NS	10.71	7.07	6.59	1.32E-17	9.97E-18 ± 1.59E-18
		8_EW					5.51E-18 ± 8.78E-19
B7		8_V					5.50E-18 ± 3.86E-19
		7_NS	15.37	10.22	8.38		1.08E-17 ± 1.06E-18
B6.2		C62V	7.93	21.74	9.51	1.22E-17	5.27E-18 ± 1.18E-18
		C62H2				2.10E-17	1.94E-18 ± 2.42E-19
		C62H1				1.19E-17	4.10E-18 ± 3.80E-19
B6.1		C61V				1.23E-17	
		C61H2	24.35	14.68	9.15	1.41E-17	8.14E-18 ± 9.33E-19
		6_NS	39.46	22.77	13.11	1.43E-17	8.60E-18 ± 5.21E-19
B5		C5H2	37.13	21.56	12.93	1.58E-17	7.27E-18 ± 6.73E-19
		C5V				1.32E-17	6.32E-18 ± 6.01E-19
		5_NS	33.51	18.46	12.01	1.45E-17	6.77E-18 ± 4.39E-19
		5_V					7.62E-18 ± 4.78E-19
B4		4_NS	37.38	23.61	12.75		1.08E-17 ± 1.92E-18
		4_2_NS					
B3		3_EW	32.57	18.92	11.78		3.49E-18 ± 1.92E-19
B2		2_NS	31.37	17.46	11.33		6.25E-18 ± 9.53E-19
B1	D	1D_NS	14.08	10.46	7.56		8.72E-18 ± 1.11E-18
B1	C	1C_NS	13.49	7.16	6.65		7.92E-18 ± 8.27E-19
B1	B2	1B_2_NS					
B1	B1	1B_1_NS	13.08	9.23	7.45		4.64E-18 ± 5.58E-19
B1	A	1A_NS	10.77	6.07	6.07		6.67E-18 ± 1.12E-18
B1	F	1F_NS	23.56	13.90	9.31		5.89E-18 ± 1.42E-18
B1	E	1E_NS	8.67	7.22	6.47		4.98E-18 ± 5.00E-19
B1	G	1G_NS	8.96	7.51	6.43		4.61E-18 ± 6.92E-19
B1	H	1H_NS	15.75	10.00	7.76		7.63E-18 ± 1.25E-18
B1		1_NS	11.59	6.87	6.58		4.21E-18 ± 7.84E-19
		1_EW					6.10E-18 ± 7.87E-19
		1_V					1.01E-17 ± 2.58E-19
B0		0_V	11.94	9.76	7.86		1.06E-17 ± 1.04E-18
B-1		-1_NS					8.41E-18 ± 8.89E-20
Number of measurements			24	24	24	16	34

* The plugs with bold labels contain clear stylolites at macroscale. The plug label extensions NS, EW, or V refer to the orientation of the plugs

Table 5 Relative porosity ($\Delta\Phi/\Phi$) and permeability ($\Delta k/k$) changes for the investigated rock at a depth of ~ 2 kmTVD with an assumed vertical effective stress of $dp \approx 25$ MPa (according to Drews et al. 2020), calculated after Eqs. (18) and (20), respectively

Plug	$\Delta\Phi/\Phi$		$\Delta k/k$			
	G^{dyn}	G^{stat}	G^{dyn}		G^{stat}	
			Δk_{Min}	Δk_{Max}	Δk_{Min}	Δk_{Max}
[-]	[%]	[%]	[%]	[%]	[%]	[%]
10_V	0.08	0.13	2.14	3.48	3.64	5.89
9_V	0.07	0.13	2.10	3.40	3.56	5.75
9_2V	0.07	0.11	1.89	3.07	3.19	5.17
C91V	0.08	0.14	2.24	3.64	3.82	6.17
C91H	0.08	0.14	2.23	3.62	3.79	6.13
C92H	0.08	0.14	2.21	3.60	3.77	6.10
8_V	0.07	0.12	1.94	3.16	3.28	5.32
C8V	0.07	0.13	2.11	3.42	3.58	5.78
C8H	0.07	0.12	2.00	3.25	3.38	5.47
7_V	0.07	0.12	1.94	3.16	3.29	5.32
C62V	0.08	0.13	2.16	3.51	3.68	5.95
C62H1	0.08	0.13	2.15	3.49	3.65	5.90
C62H2	0.07	0.12	2.06	3.34	3.49	5.65
C61V	0.07	0.12	2.02	3.28	3.42	5.54
C61H2	0.08	0.14	2.27	3.69	3.88	6.26
5_V	0.07	0.12	1.98	3.22	3.35	5.42
C5V	0.08	0.14	2.24	3.64	3.82	6.17
C5H2	0.08	0.13	2.18	3.54	3.71	6.00
4_V	0.07	0.12	1.94	3.15	3.28	5.31
4_2V	0.07	0.12	1.93	3.14	3.27	5.29
3_V	0.07	0.11	1.89	3.08	3.20	5.18
2_V	0.07	0.12	2.02	3.29	3.43	5.54
1D_V	0.06	0.11	1.81	2.95	3.06	4.95
1C_V	0.07	0.11	1.99	3.23	3.37	5.45
1A_V	0.07	0.13	2.07	3.37	3.52	5.69
1F_V	0.07	0.12	1.99	3.24	3.37	5.46
1E_V	0.06	0.11	1.77	2.87	2.97	4.82
1E_2V	0.07	0.12	1.91	3.10	3.23	5.22
1G_V	0.06	0.11	1.76	2.87	2.97	4.81
1H_V	0.07	0.12	1.93	3.14	3.27	5.29
1_V	0.07	0.11	1.85	3.01	3.12	5.05
0_V	0.06	0.10	1.65	2.69	2.77	4.50
-1_V	0.07	0.12	2.05	3.33	3.47	5.61

Abbreviations

A	Empirical parameter
$a1$	Empirical parameter
$a2$	Empirical parameter
BIB-SEM	Broad ion beam scanning electron microscopy
c	Kozeny parameter
C	Empirical parameter
cf	Converting factor
CT	Capillary tube
C_w	Empirical parameter
d	Core thickness
D	Empirical parameter
d_{cap}	Diameter of the capillary
E^{dyn}	Dynamic Young's Modulus
EGS	Enhance geothermal system
G^{dyn}	Dynamic Shear Modulus
GD	Gamma density
G^{stat}	Static Shear Modulus
I	Number of transmitted gamma photons passing unattenuated through the core
I_0	Gamma source intensity
K_b	Bohnsack permeability
K_D	Dastidar permeability
K^{dyn}	Dynamic Bulk Modulus
K_{GPPT}	GPPT permeability
K_{H-P}	Hagen-Poiseuille permeability
K_{K-C}	Kozeny-Carman permeability
K_{KT}	Katz-Thompson permeability
K_{Pre}	Predicted permeability
K_S	Saki permeability
K_W	Winland permeability
l	Pore Diameter
l_c	Critical length
l_h^{max}	Maximum hydraulic length
LMI-BIB-SEM	Liquid metal injection broad ion beam scanning electron microscopy
mD	MilliDarcy
m_{dry}	Dry mass
MICP	Mercury intrusion capillary pressure
m_{im}	Weight of submerged sample
m_{sat}	Saturated mass
MSCL	Multi-sensor core logger
NMR	Nuclear magnetic resonance
P	Pressure
P_{conf}	Confining pressure
P_i	Atmospheric pressure
P_{inj}	Injection pressure
PPR	Practical pore resolution
r_{35}	Pore diameter at 35% mercury saturation
rfn	Rock-fabric number
RGPZ	Revil-Glover-Pezard-Zamora
r_i	Hydraulic radius of each segmented pore in the BIB-SEM image
R_i	Pore throat radius at the i th capillary pressure
r_{main}	Pore diameter at maximum mercury intrusion
r_{wgm}	Geometric mean of pore throat radius
se2	Secondary electron detector
SGMB	South German Molasse Basin
TVD	True vertical depth
URG	Upper Rhine Graben
V_p	P-wave velocity
V_s	S-wave velocity
V_{tot}	Total volume of sample
β	Stress sensitivity exponent
γ	Surface tension of liquid
θ	Contact angle of liquid
μ	Compton attenuation coefficient
ν^{dyn}	Dynamic Poisson's number
ρ_{air}	Air density
ρ_{bulk}	Bulk density
ρ_{matrix}	Matrix density
τ	Tortuosity factor
Φ	Porosity
Φ_{eff}	Effective porosity

Φ_i	Porosity of each segmented pore in the BIB-SEM image
Φ_{ip}	Fractional interparticle porosity
$\Delta\Phi$	Relative porosity change

Acknowledgements

The authors as well as the whole PERMEA team sincerely thank the manager of the Simmelsdorf quarry, Richard Bärnreuther, and his staff for providing access to the sampling area and for their strong support. Also, the assistance of Lothar Ahrensmeier, Werner Kraus, Robert Sobott, and Alexandra Amann helped significantly during processing the samples and their petrophysical analysis.

Author contributions

SF conducted the sampling, sample preparation, as well as the majority of the petrophysical and geomechanical measurements and permeability modeling, data analysis, and interpretation. He also was primarily responsible for drafting this work. JK conducted the microstructural investigations and contributed significantly to the permeability modeling, data analysis, data interpretation, drafting, and structuring of this work. IM conducted some of the petrophysical measurements and helped improve the quality of this work. NK substantially contributed by providing access to the MSCL and thoroughly revising and structuring this work. JU helped in designing the project, contributed to fieldwork and discussion of the results, and contributed to writing, discussing, and revising the manuscript. HS substantially contributed by thoroughly revising and structuring this work. WB designed the project and significantly helped in improving the quality of this work by revising the manuscript. JS designed the project, applied for the funding, and substantially contributed by thoroughly revising this work. All the authors read and approved the final manuscript.

Funding

Open Access funding enabled and organized by Projekt DEAL. This project was funded by the federal Ministry of Education and Research (BMBF) within the technical program "GEO-N – Geoforschung für Nachhaltigkeit" project "PERMEA" (Grant No. 03G0865D).

Availability of data and materials

The data sets used and/or analyzed during the current study are available from the corresponding author on reasonable request.

Declarations

Ethics approval and consent to participate

This research does not involve any human subjects, human material, or human data.

Competing interests

All the authors declare that they have no conflicts of interest.

Received: 30 May 2022 Accepted: 16 November 2022

Published online: 19 December 2022

References

- Abell A, Willis K, Lange D. Mercury intrusion porosimetry and image analysis of cement-based materials. *J Colloid Interface Sci.* 1999;211:39–44.
- Agosta F, Wilson C, Aydin A. The role of mechanical stratigraphy on normal fault growth across a Cretaceous carbonate multi-layer, Central Texas (USA). *Ital J Geosci.* 2015;134:1–19. <https://doi.org/10.3301/IJG.2014.20>.
- Akanji L, Nasr G, Bageri M. Core-scale characterisation of flow in tight Arabian formations. *J Pet Explor Prod Technol.* 2013;3(4):233–41.
- Al-Obaid R, Al-Thawad FM, Gill HS. Identifying, characterizing, and locating conductive fault(s): Multiwell test analysis approach. In: Al-Obaid R, editor. *SPE asia pacific oil and gas conference and exhibition, Jakarta, Indonesia, 5–7 April 2005*. Richardson: OnePetro; 2005.
- Antonellini M, Tondi E, Agosta F, Aydin A, Cello G. Failure modes in deep-water carbonates and their impact for fault development: Majella Mountain, Central Apennines, Italy. *Mar Pet Geol.* 2008;25:1074–96. <https://doi.org/10.1016/j.marpetgeo.2007.10.008>.
- Antonellini M, Petracchini L, Billi A, Scrocca D. First reported occurrence of deformation bands in a platform limestone, the Jurassic Calcare Massiccio Fm., northern Apennines, Italy. *Tectonophysics.* 2014;628:85–104. <https://doi.org/10.1016/j.tecto.2014.04.034>.
- Armstrong RT, Sun C, Mostaghimi P, Berg S, Rucker M, Luckham P, Georgiadis A, McClure JE. Multiscale characterization of wettability in porous media. *Transp Porous Media.* 2021;140:215–40. <https://doi.org/10.1007/s11242-021-01615-0>.
- Bachmann GH, Müller M. Sedimentary and structural evolution of the German Molasse Basin. *Eclogae Geol Helv.* 1992;85:519–30. <https://doi.org/10.5169/SEALS-167019>.
- Bachmann G, Müller M, Weggen K. Evolution of the Molasse Basin (Germany, Switzerland). *Tectonophysics.* 1987;137:77–92.
- Bakhtiari HA, Moosavi A, Kazemzadeh E, Kamran G, Esfahani MR, Vali J. The effect of rock types on pore volume compressibility of limestone and dolomite samples. *Geopersia.* 2011;1(1):37–82. <https://doi.org/10.22059/jgeope.2011.22163>.
- Barri AA, Hassan AM, Aljawad MS, Mahmoud M. Effect of treatment conditions on matrix stimulation of carbonate rocks with chelating agents. *Arab J Sci Eng.* 2021. <https://doi.org/10.1007/s13369-021-05633-4>.

- Bastos AC, Dillon LD, Vasquez GF, Soares JA. Core derived acoustic, porosity and permeability correlations for computation pseudo-logs. In: Harvey PK, Lovell MA, editors. Core-log integration. London: Geological Society; 1998. p. 141–6.
- Beichel K, Koch R, Wolfgramm M. Die Analyse von Spülproben zur Lokalisierung von Zuflusszonen in Geothermiebohrungen. Beispiel der Bohrungen Gt Unterhaching 1/1a und 2. (Süddeutschland, Molassebecken, Malm). *Geol BI NO-Bayern*. 2014;64(1–4):43–65.
- Bertoncello A, Honarpour MM. Standards for characterization of rock properties in unconventional reservoirs: fluid flow mechanism, quality control, and uncertainties. In: Bertoncello A, editor. SPE Annual technical conference and exhibition, New Orleans, Louisiana, U.S.A., 30 September–2 October 2013. Richardson: OnePetro; 2013.
- Böhm F, Koch R, Höferle R, Baasch R. Der Malm in der Geothermiebohrung Pullach Th2 - Faziesanalyse aus Spülproben (München, S-Deutschland). *Geol BI NO-Bayern*. 2010;60(1–4):79–112.
- Bohsack D, Potten M, Pfrang D, Wolpert P, Zosseder K. Porosity–permeability relationship derived from Upper Jurassic carbonate rock cores to assess the regional hydraulic matrix properties of the Malm reservoir in the South German Molasse Basin. *Geotherm Energy*. 2020;8(12):1–47.
- Bohsack D, Potten M, Freitag S, Einsiedl F, Zosseder K. Stress sensitivity of porosity and permeability under varying hydrostatic stress conditions for different carbonate rock types of the geothermal Malm reservoir in Southern Germany. *Geotherm Energy*. 2021;9(15):1–59.
- Boulin PF, Bretonnier P, Gland N, Lombard JM. Contribution of the steady state method to water permeability measurement in very low permeability porous media. *Oil Gas Sci Technol*. 2012;67(3):387–401.
- Bruna P, Lavenu A, Matonti C, Bertotti G. Are stylolites fluid-flow efficient features? *J Struct Geol*. 2019;125:270–7.
- Burgess C, Peter C. Formation, Distribution, and Prediction of Stylolites as Permeability Barriers in the Thamama Group Abu Dhabi. In: Burgess C, editor. SPE Proceedings middle east oil technical conference and exhibition, Bahrain 11–14 March 1985. Richardson: OnePetro; 1985.
- Cai J, Zhang Z, Wei W, Guo D, Li S, Zhao P. The critical factors for permeability-formation factor relation in reservoir rocks: Pore-throat ratio, tortuosity and connectivity. *Energy*. 2019;188:1–10.
- Carman P. Fluid flow through granular beds. *Chem Eng Res Des*. 1937;75:32–48.
- Chenevert ME, Sharma AK. Permeability and effective pore pressure of shales. *SPE Drill Complet*. 1993;8:28–34.
- Cheng AH. Poroelasticity: theory and applications of transport in porous media. Cham: Springer; 2016.
- Clarkson CR, Solano N, Bustin RM, Bustin AMM, Chalmers GRL, He L, Melnichenko YB, Radliński AP, Blach TP. Pore structure characterization of North American shale gas reservoirs using USANS/SANS, gas adsorption, and mercury intrusion. *Fuel*. 2013;103:606–16.
- Cohen KM, Finney SC, Gibbard PL, Fan J-X. The ICS International Chronostratigraphic chart, international commission on stratigraphy. *Episodes*. 2013;36:199–204.
- Comisky JT, Newsham KE, Rushing JA, Blasingame TA. A Comparative Study of Capillary-Pressure-Based Empirical Models for Estimating Absolute Permeability in Tight Gas Sands. In: SPE Annual Technical Conference and Exhibition, Anaheim, California, U.S.A., 11–14 November 2007. 2007.
- Dastidar R, Sondergeld C, Rai C. An improved empirical permeability estimator from mercury injection for tight clastic rocks. *Petrophysics*. 2007;48(3):186–90.
- David C, Wong T, Zhu W, Zhang J. Laboratory measurement of compaction-induced permeability change in porous rocks: Implications for the generation and maintenance of pore pressure excess in the crust. *PAGEOPH*. 1994;143(1–3):425–56. <https://doi.org/10.1007/BF00874337>.
- Dimmen V, Rotevatn A, Peacock DCP, Nixon CW, Nærland K. Quantifying structural controls on fluid flow: insights from carbonate-hosted fault damage zones on the Maltese Islands. *J Struct Geol*. 2017;101:43–57.
- Drews MC, Hofstetter P, Zosseder K, Straubinger R, Gahr A, Stollhofen H. Predictability and controlling factors of overpressure in the North Alpine Foreland Basin, SE Germany: an interdisciplinary post-drill analysis of the Geretsried GEN-1 deep geothermal well. *Geotherm Energy*. 2020;8(20):1–24. <https://doi.org/10.1186/s40517-020-00175-8>.
- Du S. Prediction of permeability and its anisotropy of tight oil reservoir via precise pore-throat tortuosity characterization and “umbrella deconstruction” method. *J Pet Sci Eng*. 2019;178:1018–28. <https://doi.org/10.1016/j.petrol.2019.03.009>.
- Eberli GP, Baechele GT, Anselmetti FS, Incze ML. Factors controlling elastic properties in carbonate sediments and rocks. *Lead Edge*. 2003;22(7):654–60. <https://doi.org/10.1190/1.1599691>.
- Fazlikhani H, Bauer W, Stollhofen H. Variscan structures and their control on latest to post-Variscan basin architecture: insights from the westernmost Bohemian Massif and SE Germany. *Solid Earth*. 2022;13:393–416. <https://doi.org/10.5194/se-13-393-2022>.
- Fens TW. Petrophysical properties from small rock samples using image analysis techniques [Dissertation]. TU Delft: Technical University Delft; 2000.
- Filomena CM, Stollhofen H. Ultrasonic logging across unconformities—outcrop and core logger sonic patterns of the Early Triassic Middle Buntsandstein Hardegsen unconformity, southern Germany. *Sed Geol*. 2011;236(3–4):185–96.
- Freitag S, Drews M, Bauer W, Duschl F, Misch D, Stollhofen H. Cretaceous paleo-thicknesses in Central Europe: new insights from shale compaction and thermal history analyses on the Franconian Alb. *SE Germany Solid Earth*. 2022;13:1003–26. <https://doi.org/10.5194/se-13-1003-2022>.
- Gao H, Li T, Yang L. Quantitative determination of pore and throat parameters in tight oil reservoir using constant rate mercury intrusion technique. *J Pet Explor Prod Technol*. 2016;6(2):309–18.
- Giesche H. Mercury porosimetry: a general (practical) overview. *Part Part Syst Charact*. 2006;23(1):9–19.
- Gosnold W, Lefever R, Mann M, Klennner R, McDonald M, Salehfar H. EGS potential in the northern midcontinent of North America. *Geotherm Resour Counc Trans*. 2010;34:355–8.
- Graham B, Antonellini M, Aydin A. Formation and growth of normal faults in carbonates within a compressive environment. *Geology*. 2003;31:11–4. [https://doi.org/10.1130/0091-7613\(2003\)031%3C0011:FAGONF%3E2.0.CO;2](https://doi.org/10.1130/0091-7613(2003)031%3C0011:FAGONF%3E2.0.CO;2).
- Gunter GW, Spain DR, Viro EJ, Thomas JB, Potter G, Williams J. Winland pore throat prediction method - A proper retrospect: New examples from carbonates and complex systems. In: SPWLA 55th Annual Logging Symposium, Abu Dhabi, United Arab Emirates, May 2014. 2014.

- Haines TJ, Michie EAH, Neilson JE, Healy D. Permeability evolution across carbonate hosted normal fault zones. *Mar Pet Geol.* 2016;72:62–82.
- Hall C, Hamilton A. Porosities of building limestones: using the solid density to assess data quality. *Mater Struct.* 2016;49(10):3969–79.
- Heap MJ, Baud P, Reuschlé T, Meredith PG. Stylolites in limestones: barriers to fluid flow? *Geology.* 2014;42(1):51–4.
- Hofmann H, Weides S, Babadagli T, Zimmermann G, Moeck I, Majorowicz J, Unsworth M. Potential for enhanced geothermal systems in Alberta, Canada. *Energy.* 2014;69:578–91.
- Homuth S, Sass I. Outcrop analogue vs. reservoir data: characteristics and controlling factors of physical properties of the upper jurassic geothermal carbonate reservoirs of the Molasse Basin, Germany. In: Thirty-Eighth Workshop on Geothermal Reservoir Engineering; 24–26 February 2014; Stanford, California; 2014.
- Homuth S, Götz AE, Sass I. Lithofacies and depth dependency of thermo- and petrophysical rock parameters of the Upper Jurassic geothermal carbonate reservoirs of the Molasse Basin. *Zeitschrift Der Deutschen Gesellschaft Für Geowissenschaften.* 2014;165(3):469–86. <https://doi.org/10.1127/1860-1804/2014/0074>.
- Homuth S, Götz AE, Sass I. Reservoir characterization of the Upper Jurassic geothermal target formations (Molasse Basin, Germany): role of thermofacies as exploration tool. *Geotherm Energy.* 2015;3(1):41–9. <https://doi.org/10.5194/gtes-3-41-2015>.
- Hu Z, Klaver J, Schmatz J, Dewanckele J, Littke R, Krooss BM, Amann-Hildenbrand A. Stress sensitivity of porosity and permeability of Cobourg limestone. *Eng Geol.* 2020;273: 105632. <https://doi.org/10.1016/j.enggeo.2020.105632>.
- Jennings JW, Lucia FJ. Predicting permeability from well logs in carbonates with a link to geology for interwell permeability mapping. *SPE Reserv Eval Eng.* 2003;6(4):215–25. <https://doi.org/10.1016/j.enggeo.2020.105632>.
- Katsube TJ, Mudford BS, Best ME. Petrophysical characteristics of shales from the Scotian Shelf. *Geophysics.* 1991;56:1681–9.
- Katz AJ, Thompson AH. Quantitative prediction of permeability in porous rock. *Phys Rev B.* 1986;34(11):8179–81.
- Katz AJ, Thompson AH. Prediction of rock electrical conductivity from mercury injection measurements. *J Geophys Res.* 1987;92(B1):599–607.
- Kiula U, McCarty DK, Derkowski A, Fischer TB, Prasad M. Total porosity measurement in gas shales by the water immersion porosimetry (WIP) method. *Fuel.* 2014;117:1115–29. <https://doi.org/10.1016/j.fuel.2013.09.073>.
- Klaver J, Desbois G, Urai JL, Littke R. BIB-SEM study of the pore space morphology in early mature Posidonia Shale from the Hils area, Germany. *Int J Coal Geol.* 2012;103:12–25. <https://doi.org/10.1016/j.coal.2012.06.012>.
- Klaver J, Hemes S, Houben M, Desbois G, Radi Z, Urai JL. The connectivity of pore space in mudstones: insights from high-pressure Wood's metal injection, BIB-SEM imaging, and mercury intrusion porosimetry. *Geofluids.* 2015;15(4):577–91. <https://doi.org/10.1111/gfl.12128>.
- Kley J, Voigt T. Late Cretaceous intraplate thrusting in central Europe: effect of Africa-Iberia-Europe convergence, not Alpine collision. *Geology.* 2008;36:839–42. <https://doi.org/10.1130/G24930A>.
- Klinkenberg LJ. The permeability of porous media to liquid and gases. *Drill Prod Pract.* 1941;2:200.
- Koch R, Weiss C. Field Trip A: Basin-Platform Transitions in Upper Jurassic Limestones and Dolomites of the Northern Franconian Alb (Germany). *Zitteliana.* 2005;26:43–56.
- Koehler S, Duschl F, Fazlikhani H, Köhn D, Stephan T, Stollhofen H. Reconstruction of cyclic Mesozoic-Cenozoic stress development in SE Germany using fault-slip and stylolite inversion. *Geol Mag.* 2022. <https://doi.org/10.1017/S0016756822000656>.
- Koehn D, Rood MP, Beaudoin N, Chung P, Bons PD, Gomez-Rivas E. A new stylolite classification scheme to estimate compaction and local permeability variations. *Sediment Geol.* 2016;346:60–71. <https://doi.org/10.1016/j.sedgeo.2016.10.007>.
- Korneva I, Tondi E, Agosta F, Rustichelli A, Spina V, Bitonte R, Di Cuia R. Structural properties of fractured and faulted Cretaceous platform carbonates, Murge Plateau (southern Italy). *Mar Pet Geol.* 2014;57:312–26. <https://doi.org/10.1016/j.marpetgeo.2014.05.004>.
- Kozeny J. Über kapillare Leitung des Wassers im Boden: Sitzungsberichte der Wiener Akademie der Wissenschaften. *Wiener Akademie Der Wissenschaften.* 1927;136:271–306.
- Lala AMS, El-Sayed NAA. Controls of pore throat radius distribution on permeability. *J Pet Sci Eng.* 2017;157:941–50. <https://doi.org/10.1016/j.marpetgeo.2014.05.004>.
- Li Z, Wu S, Xia D, He S, Zhang X. An investigation into pore structure and petrophysical property in tight sandstones: a case of the Yanchang Formation in the southern Ordos Basin, China. *Mar Pet Geol.* 2018;97:390–406. <https://doi.org/10.1016/j.marpetgeo.2018.07.014>.
- Litsey LR, MacBride WL, Al-Hinai KM, Dismukes NB. Shuaiba reservoir geological study, Yibal field, Oman. *J Pet Technol.* 1986;38(06):651–61. <https://doi.org/10.2118/11454-PA>.
- Lucia FJ. Rock-fabric/petrophysical classification of carbonate pore space for reservoir characterization. *AAPG Bull.* 1995;79(9):1275–300. <https://doi.org/10.1306/7834D4A4-1721-11D7-8645000102C1865D>.
- Lucia FJ. Permeability and rock fabric from wireline logs, Arab-D reservoir, Ghawar field, Saudi Arabia. *Geoarabia.* 2001;6(4):619–46.
- Mehrabi H, Mansouri M, Rahimpour-Bonab H, Tavakoli V, Hassanzadeh M. Chemical compaction features as potential barriers in the Permian-Triassic reservoirs of Southern Iran. *J Pet Sci Eng.* 2016;145:95–113.
- Meyer RKF. Stratigraphie und Fazies des Frankendolomits (Malm) 2. Teil: Mittlere Frankenalb. *Erlanger Geol Abh.* 1974;96:3–35.
- Meyer RKF. Kreide. In: Freudenberger W, Schwerd K, editors. Erläuterungen zur Geologischen Karte 1:500000 Bayern. München: Bayerisches Geologisches Landesamt; 1996. p. 112–28.
- Micarelli L, Benedicto A, Invernizzi C, Saint-Bezar B, Michelot JL, Vergely P. Influence of P/T conditions on the style of normal fault initiation and growth in limestones from the SE-Basin, France. *J Struct Geol.* 2005;27:1577–98. <https://doi.org/10.1016/j.jsg.2005.05.004>.
- Michie EAH. Influence of host lithofacies on fault rock variation in carbonate fault zones: a case study from the Island of Malta. *J Struct Geol.* 2015;76:61–79. <https://doi.org/10.1016/j.jsg.2015.04.005>.

- Moekel IS, Düssel M, Weber J, Schintgen T, Wolfgramm M. Geothermal play typing in Germany, case study Molasse Basin: a modern concept to categorise geothermal resources related to crustal permeability. *Neth J Geosci*. 2019;98:1–10. <https://doi.org/10.1017/njg.2019.12>.
- Moosavi SA, Goshtasbi K, Kazemzadeh E, Bakhtiari HA, Esfahani MR, Vali J. Relationship between porosity and permeability with stress using pore volume compressibility characteristic of reservoir rocks. *Arab J Geosci*. 2014;7(1):231–9. <https://doi.org/10.1007/s12517-012-0760-x>.
- Mraz E. Reservoir characterization to improve exploration concepts of the Upper Jurassic in the Southern Bavarian Molasse Basin [Dissertation]. TU München: Technical University of Munich; 2019.
- Mraz E, Bohnsack D, Stockinger G, Käsling H, Zosseder K, Thuro K. Die Bedeutung von Analogaufschlüssen des Oberjura für die Interpretation der Lithologie der geothermalen Tiefbohrung Geretsried. *Jahresberichte Und Mitteilungen Des Oberrheinischen Geologischen Vereins*. 2018;100:517–47.
- Nenna F, Aydin A. The formation and growth of pressure solution seams in clastic rocks: a field and analytical study. *J Struct Geol*. 2011;33(4):633–43. <https://doi.org/10.1016/j.jsg.2011.01.014>.
- Newsham KE, Rushing JA, Lasswell PM, Cox JC, Blasingame TA. A comparative study of laboratory techniques for measuring capillary pressures in tight gas sands. In: SPE annual technical conference and exhibition, Houston, Texas, U.S.A., 26–29 September 2004. 2004.
- Nishiyama N, Yokoyama T. Estimation of permeability of sedimentary rocks by applying water-expulsion porosimetry to Katz and Thompson model. *Eng Geol*. 2014;177:75–82. <https://doi.org/10.1306/070615142056>.
- O'Neill N. Fahud field review: a switch from water to gas injection. *J Pet Technol*. 1988;40(05):609–18. <https://doi.org/10.1306/070615142056>.
- Okolo GN, Everson RC, Neomagus HWJP, Roberts MJ, Sakurovs R. Comparing the porosity and surface areas of coal as measured by gas adsorption, mercury intrusion and SAXS techniques. *Fuel*. 2015;141:293–304. <https://doi.org/10.1306/070615142056>.
- Pei L, Rühaak W, Stegner J, Bär K, Homuth S, Miel P, Sass I. Thermo-Triax: an apparatus for testing petrophysical properties of rocks under simulated geothermal reservoir conditions. *Geotech Test J*. 2014;38(1):20140056. <https://doi.org/10.1520/GTJ20140056>.
- Petek A, Rauche H, Schröder B. Die strukturelle Entwicklung des E-Randes der Süddeutschen Scholle in der Kreide. *Z Geol Wiss*. 1996;24(1/2):65–77.
- Petek A, Rauche H, Schröder B, Franzke H-J, Bankwitz P, Bankwitz E. The late- and post-Variscan tectonic evolution of the Western Border fault zone of the Bohemian massif (WBZ). *Geol Rundschau*. 1997;86:191–202.
- Pharaoh TC, Duser M, Geluk MC, Kockel F, Krawczyk CM, Krzywiec P, Scheck-Wenderoth M, Thybo H, Vejbaek OV, Van Wees JD. Tectonic evolution. In: Doornenbal H, Stevenson AG, editors. *Petroleum Geological Atlas of the Southern Permian Basin Area*. Utrecht: TNO Geological Survey of the Netherlands; 2010. p. 25–57.
- Philipp T, Amann-Hildenbrand A, Laurich B, Desbois G, Littke R, Urai JL. The effect of microstructural heterogeneity on pore size distribution and permeability in Opalinus Clay (Mont Terri, Switzerland): insights from an integrated study of laboratory fluid flow and pore morphology from BIB-SEM images. *Geol Soc Lond Special Publ*. 2017;454(1):85–106. <https://doi.org/10.1144/SP454.3>.
- Pieńkowski G, Schudack ME, Bosák P, Enay R, Feldman-Olszewska A, Golonka J, Gutowski J, Hergreen GFW, Jordan P, Krobicki M, Lathuiliere B, Leinfelder RR, Michalik J, Mönnig E, Noe-Nygaard N, Pálffy J, Pint A, Rasser MW, Reisdorf AG, Schmid DU, Schweigert G, Surlyk F, Wetzel A, Wong TE. In: McCann T, editor. *The Geology of Central Europe. Volume 2: Mesozoic and Cenozoic*, London: The Geological Society of London; 2008. p. 823–922.
- Potten M. Geomechanical characterization of sedimentary and crystalline geothermal reservoir [Dissertation]. TU Munich: Technical University of Munich; 2020.
- Potten M, Sellmeier B, Mraz E, Thuro K. Geomechanical Investigation of High Priority Geothermal Strata in the Molasse Basin, Bavaria, Germany. In: Shakoar A, Cato K, editors. *IAEG/AEG Annual Meeting Proceedings, San Francisco, California, vol. 2*. Cham: Springer; 2019. p. 21–6. https://doi.org/10.1007/978-3-319-93127-2_4.
- Rashid F, Glover PWJ, Lorinczi P, Hussein D, Collier R, Lawrence J. Permeability prediction in tight carbonate rocks using capillary pressure measurements. *Mar Pet Geol*. 2015;68:536–50. <https://doi.org/10.1016/j.marpetgeo.2015.10.005>.
- Rashid F, Glover PWJ, Lorinczi P, Hussein D, Lawrence J. Microstructural controls on reservoir quality in tight oil carbonate reservoir rocks. *J Pet Sci Eng*. 2017;156:814–26. <https://doi.org/10.1016/j.petrol.2017.06.056>.
- Reicherter K, Froitzheim N, Jarosiński M, Badura J, Franzke H-J, Hansen M, Hübscher C, Müller R, Poprawa P, Reinecker J, Stackebrandt W, Voigt T, von Eynatten H, Zuchiewicz W. Alpine tectonics north of the Alps. In: McCann T, editor. *The Geology of Central Europe, Mesozoic and Cenozoic, vol. 2*. Bonn: The Geological Society London; 2008. p. 1233–86.
- Sagi DA, De Paola N, McCaffrey KJW, Holdsworth RE. Fault and fracture patterns in low porosity chalk and their potential influence on sub-surface fluid flow—a case study from Flamborough Head, UK. *Tectonophysics*. 2016;690:35–51. <https://doi.org/10.1016/j.tecto.2016.07.009>.
- Saki M, Siahpoush S, Khaz'ali AR. A new generalized equation for estimation of sandstone and carbonate permeability from mercury intrusion porosimetry data. *J Pet Explor Prod Technol*. 2020;10(7):2637–44. <https://doi.org/10.1007/s13202-020-00900-w>.
- Sander R, Pan Z, Connell LD. Laboratory measurement of low permeability unconventional gas reservoir rocks: a review of experimental methods. *J Nat Gas Sci Eng*. 2017;37:248–79. <https://doi.org/10.1016/j.jngse.2016.11.041>.
- Scheck-Wenderoth M, Krzywiec P, Zühlke R, Maystrenko Y, Froitzheim N. Permian to Cretaceous tectonics. In: McCann T, editor. *The Geology of Central Europe, Mesozoic and Cenozoic, vol. 2*. Bonn: The Geological Society London; 2008. p. 999–1030.
- Schön JP. *Physical properties of rocks: fundamentals and principles of petrophysics*. Amsterdam: Elsevier; 2015.
- Schröder B. Zur Morphogenese im Ostteil der Süddeutschen Scholle. *Geol Rundschau*. 1968;58:10–32.
- Schröder B. Inversion tectonics along the western margin of the Bohemian Massif. *Tectonophysics*. 1987;137:93–100.

- Selvadurai APS, Głowacki A. Permeability hysteresis of limestone during isotropic compression. *Ground Water*. 2008;46(1):113–9. <https://doi.org/10.1111/j.1745-6584.2007.00390.x>.
- Shi Y, Wang CY. Pore pressure generation in sedimentary basins: overloading versus aquathermal. *J Geophys Res Solid Earth*. 1986;91(B2):2153–62.
- Si L, Li Z, Yang Y. Influence of the pore geometry structure on the evolution of gas permeability. *Transp Porous Media*. 2018;123(2):321–39. <https://doi.org/10.1007/s11242-018-1044-z>.
- Sigal RF. A methodology for blank and conformance corrections for high pressure mercury porosimetry. *Meas Sci Technol*. 2009;20:1–11. <https://doi.org/10.1088/0957-0233/20/4/045108>.
- Sinn CJA, Klaver J, Fink R, Jiang M, Schmatz J, Littke R, Urai JL. Using BIB-SEM imaging for permeability prediction in heterogeneous shales. *Geofluids*. 2017. <https://doi.org/10.1155/2017/4709064>.
- Smodej J, Lemmens L, Reuning L, Hiller T, Klitzsch N, Claes S, Kukla PA. Nano- to millimeter scale morphology of connected and isolated porosity in the Permo-Triassic Khuff formation of Oman. *Geosciences*. 2020;10(7):1–29. <https://doi.org/10.3390/geosciences10010007>.
- Stober I, Bucher K. *Geothermal Energy*. Berlin: Springer-Verlag; 2013. <https://doi.org/10.1007/978-3-642-13352-7>.
- Tondi E. Nucleation, development and petrophysical properties of faults in carbonate grainstones: Evidence from the San Vito Lo Capo peninsula (Sicily, Italy). *J Struct Geol*. 2007;29:614–28. <https://doi.org/10.1016/j.jsg.2006.11.006>.
- Toussaint R, Aharonov E, Koehn D, Gratier J-P, Ebner M, Baud P, Rolland A, Renard F. Stylolites: a review. *J Struct Geol*. 2018;114:163–95. <https://doi.org/10.1016/j.jsg.2018.05.003>.
- Vandeginste V, John CM. Diagenetic implications of stylolitization in pelagic carbonates, Canterbury basin, offshore New Zealand. *J Sediment Res*. 2013;83:226–40. <https://doi.org/10.2110/jsr.2013.18>.
- Vejbæk OV, Andersen C, Dusar M, Herrngreen GFW, Krabbe H, Leszczyński K, Lott GK, Mutterlose J, Van der Molen AS. Cretaceous. In: Doornenbal H, Stevenson AG, editors. *Petroleum geological atlas of the southern Permian Basin Area*. Utrecht: TNO Geological Survey of the Netherlands; 2010. p. 195–209.
- Voigt S, Aurag A, Leis F, Kaplan U. Late Cenomanian to Middle Turonian high-resolution carbon isotope stratigraphy: new data from the Münsterland Cretaceous Basin. *Germany Earth Planet Sci Lett*. 2007;253:196–210. <https://doi.org/10.1016/j.epsl.2006.10.026>.
- Voigt S, Wagreich M, Surlyk F, Walaszczyk I, Uličný D, Čech S, Voigt T, Wiese F, Wilmsen M, Niebuhr B, Reich M, Funk H, Michalík J, Jagt JWM, Felder PJ, Schulp AS. Cretaceous. In: McCann T, editor. *The Geology of Central Europe, Mesozoic and Cenozoic*, vol. 2. Bonn: The Geological Society London; 2008. p. 923–98.
- Voigt T, Kley J, Voigt S. Dawn and dusk of Late Cretaceous basin inversion in central Europe? *Solid Earth*. 2021;12:1443–71. <https://doi.org/10.5194/se-12-1443-2021>.
- Von Eynatten H, Kley J, Dunkl I, Hoffmann V-E, Simon A. Late Cretaceous to Paleogene exhumation in central Europe—localized inversion vs. large-scale domal uplift. *Solid Earth*. 2021;12:935–58. <https://doi.org/10.5194/se-12-935-2021>.
- Wagner GA, Coyle DA, Duyster J, Henjes-Kunst F, Peterek A, Schröder B, Stöckhert B, Wemmer K, Zulauf G, Ahrendt H, Bischoff R, Hejl E, Jacobs J, Menzel D, Lal N, van den Haute P, Vercoutere C, Welzel B. Post-Variscan thermal and tectonic evolution of the KTB site and its surroundings. *J Geophys Res*. 1997;102:18221–32.
- Washburn EW. The dynamics of capillary flow. *Phys Rev*. 1921;17(3):273–83.
- Webb PA. *An Introduction To The Physical Characterization of Materials by Mercury Intrusion Porosimetry with Emphasis On Reduction And Presentation of Experimental Data*. Micromeritics Instruments Corp. 2001.
- Weber ME, Niessen F, Kuhn G, Wiedicke M. Calibration and application of marine sedimentary physical properties using a multi-sensor core logger. *Mar Geol*. 1997;136:151–72.
- Weber J, Born H, Moeck I. Geothermal energy use, country update for Germany 2016–2018. In: *European Geothermal Congress*, Den Haag, Netherland, 11–14 June 2019. 2019.
- Weger RJ, Baechle GT, Masafferro JL, Eberli GP. Effects of porestructure on sonic velocity in carbonates. In: *SEG 74th Annual Meeting*, Dallas, Texas, U.S.A., 10–15 October 2004. 2004. <https://library.seg.org/doi/10.1190/1.1845169>.
- Wu Y, Tahmasebi P, Lin C, Zahid MA, Dong C, Golab A, Ren L. A comprehensive study on geometric, topological and fractal characterization of pore systems in low-permeability reservoirs based on SEM, MICP, NMR, and X-ray CT experiments. *Mar Pet Geol*. 2019;103:12–28. <https://doi.org/10.1016/j.marpetgeo.2019.02.003>.
- Xu C, Lin C, Kang Y, You L. An experimental study on porosity and permeability stress-sensitive behavior of sandstone under hydrostatic compression: characteristics, mechanisms and controlling factors. *Rock Mech Rock Eng*. 2018a;51:2321–38. <https://doi.org/10.1007/s00603-018-1481-6>.
- Xu Y, Wang Y, Yuan H, Zhang D, Agostini F, Skoczylas F. Pore structure characterization of tight sandstone from Sbaa Basin, Algeria: Investigations using multiple fluid invasion methods. *J Nat Gas Sci Eng*. 2018b;59:414–26. <https://doi.org/10.1016/j.jngse.2018.09.021>.
- Zeiss A. Jurassic stratigraphy of Franconia. *Stuttgarter Beiträge Zur Naturkunde Serie b*. 1977;31:1–32.
- Zeybeck M, Kuchuk FJ. Fault and fracture characterization using 3D interval pressure transient tests. In: *Abu Dhabi International Petroleum Exhibition and Conference*. Abu Dhabi, United Arab Emirates, 13–16 October 2002. 2002.
- Zhao X, Yang Z, Lin W, Xiong S, Wei Y. Characteristics of microscopic pore-throat structure of tight oil reservoirs in Sichuan Basin measured by rate-controlled mercury injection. *Open Physics*. 2018;16(1):675–84. <https://doi.org/10.1515/phys-2018-0086>.
- Ziauddin ME, Bize E. The effect of pore scale heterogeneities on carbonate stimulation treatments. In: *SPE Middle East Oil and Gas Show and Conference*, Manama, Bahrain, March 11–14 2007.
- Ziegler PA. Late Cretaceous and Cenozoic intra-plate compressional deformations in the Alpine foreland—a geodynamic model. *Tectonophysics*. 1987;137:389–420.
- Ziegler PA. *Geological Atlas of Western and Central Europe*. 2nd ed. London: Geological Society Publishing House; 1990.
- Ziegler PA, Cloetingh S, van Wees JD. Dynamics of intraplate compressional deformation: the Alpine foreland and other examples. *Tectonophysics*. 1995;252:7–59.
- Zinszner B, Pellerin F-M. *A geoscientist's guide to petrophysics*. Paris: Editions Technip; 2007.

- Zoback MD, Byerlee JD. The effect of microcrack dilatancy on the permeability of westerly granite. *J Geophys Res.* 1975;80(5):752–5. <https://doi.org/10.1029/JB080i005p00752>.
- Zulauf G. Brittle deformation events at the western border of the Bohemian Massif (Germany). *Geol Rundschau.* 1993;82:489–504.

Publisher's Note

Springer Nature remains neutral with regard to jurisdictional claims in published maps and institutional affiliations.

Submit your manuscript to a SpringerOpen[®] journal and benefit from:

- ▶ Convenient online submission
- ▶ Rigorous peer review
- ▶ Open access: articles freely available online
- ▶ High visibility within the field
- ▶ Retaining the copyright to your article

Submit your next manuscript at ▶ [springeropen.com](https://www.springeropen.com)
